Discovery of a Remarkably Powerful Broad Absorption-line Quasar Outflow in SDSS J135246.37+423923.5

Hyunseop Choi[1] , Karen M. Leighly[1] , Donald M. Terndrup[1,2] , Sarah C. Gallagher[3,4,5,6], and Gordon T. Richards[7]

[1] Homer L. Dodge Department of Physics and Astronomy, The University of Oklahoma, 440 W. Brooks St., Norman, OK 73019, USA
[2] Department of Astronomy, The Ohio State University, 140 W. 18th Ave., Columbus, OH 43210, USA
[3] Department of Physics & Astronomy, The University of Western Ontario, London, ON N6A 3K7, Canada
[4] Canadian Space Agency, 6767 Route de l'Aeroport, Saint-Hubert, QC J3Y BY9, Canada
[5] Institute for Earth and Space Exploration, The University of Western Ontario, London, ON N6A 3K7, Canada
[6] The Rotman Institute of Philosophy, The University of Western Ontario, London, ON N6A 3K7, Canada
[7] Department of Physics, Drexel University, 32 S. 32nd St., Philadelphia, PA 19104, USA

Abstract

Broad absorption-line (BAL) features in quasar spectra reveal an unambiguous signature of energetic outflows from central supermassive black holes, and thus, BAL quasars are prime targets for investigating the potential process of luminous quasar feedback on galaxies. We analyzed the rest-UV spectrum of an "overlapping trough" iron low-ionization broad absorption-line quasar (FeLoBAL) SDSS J135246.37+423923.5 using the novel spectral synthesis code $SimBAL$ and discovered an extraordinarily fast and energetic BAL outflow. Our analysis revealed outflow velocities reaching $\sim -38,000$ km s^{-1} with a velocity width of $\sim 10,000$ km s^{-1}, which is the largest FeLoBAL outflow velocity measured to date. The column density of the outflow gas is $\log N_{\rm H} \sim 23.2$ (cm^{-1}) with the log kinetic luminosity $\log L_{\rm KE} \sim 48.1$ (erg s^{-1}), which exceeds the bolometric luminosity of the quasar and is energetic enough to effectively drive quasar feedback. The energy estimate for the outflow is far greater than the estimates from any BAL object previously reported. The object also shows "anomalous reddening" and a significant scattered component that we were able to model with $SimBAL$. We found the first definitive case for radiation filtering in an additional zero-velocity absorption component that required an absorbed continuum to produce the particular absorption lines observed (Mg II, Al III, and Al II) without also producing the high-ionization lines such as C IV.

Unified Astronomy Thesaurus concepts: Broad-absorption line quasar (183); Spectroscopy (1558); High-luminosity active galactic nuclei (2034); Galaxies (573)

1. Introduction

Broad absorption-line (BAL) quasars (BALQs) have been studied extensively in the past several decades since their discovery (Lynds 1967), and their distinctive blueshifted BAL features provide clear evidence for quasar outflows (e.g., Weymann et al. 1991). Once corrected for selection effects, BALQs are found in 20% ∼ 40% of the total quasar population (Foltz et al. 1990; Weymann et al. 1991; Tolea et al. 2002; Reichard et al. 2003; Trump et al. 2006; Dai et al. 2008; Knigge et al. 2008; Allen et al. 2011). BALQs are further divided into subgroups based on their spectroscopic properties. High-ionization BALQs (HiBALs) show only the absorption transitions from highly ionized atoms (C IV, Si IV, N V, O VI), while low-ionization (LoBALQs) show both the high-ionization transitions and absorption lines from lower-ionization ions (Mg II, Al II, Al III) in their rest-UV spectra. There is also another class of rarer BALQs called FeLoBALQs that show Fe II absorption lines. These objects have large gas column densities, thick enough to extend beyond the hydrogen ionization front (Hazard et al. 1987). Although FeLoBALs comprise less than ∼2% of the observed quasar population (Dai et al. 2012), their outflows can have the highest column densities compared to other types of BAL outflows (Lucy et al. 2014). Some FeLoBAL objects with broad saturated troughs, where the troughs overlap to nearly completely absorb the continuum emission shortward of 2800 Å, are called "overlapping trough" objects (e.g., Hall et al. 2002), and they are expected to have the largest hydrogen column densities (log $N_{\rm H}$) in their outflows.

Outflowing winds with energy exceeding 0.5% ∼ 5% of the quasar luminosity (e.g., Scannapieco & Oh 2004; Di Matteo et al. 2005; Hopkins & Elvis 2010) are thought to be able to effectively cause AGN feedback. Outflow energies depend on the amount of material (log $N_{\rm H}$) that is being carried by the wind, and more importantly, the velocity of the outflow through $\dot{E}_k = 8\pi \mu m_p \Omega R N_{\rm H} v^3$ (Dunn et al. 2010). The combination of large column density (log $N_{\rm H}$) and high velocity produce energetic outflows.

A few discoveries of high-velocity HiBAL outflows ($v \sim 0.1c$–$0.3c$) have been made. For example, Rodríguez Hidalgo et al. (2011) discussed a $v \sim 0.2c$ BAL outflow in PG0935+417, and Hamann et al. (2018) suggested that there is a C IV BAL feature at $v \sim 0.3c$ in PDS 456. Rogerson et al. (2016) reported BAL features at $v \sim 0.2c$ and $0.1c$ in the variable HiBALQ SDSS 0230+0059. In the cases mentioned above, the physical properties of the outflows were not sufficiently constrained to estimate the outflow energy because those HiBAL objects only showed prominent C IV absorption lines (and Si IV or N V lines in some cases) and lacked diagnostic lines to probe the density of the outflow. Moreover, HiBALQs are not expected to have the highest log $N_{\rm H}$.

LoBALQs and FeLoBALQs have significantly higher column densities, and therefore, high-velocity outflows in these objects may yield the most energetic outflows. Fynbo et al. (2020) discovered a high-velocity LoBAL outflow ($v \sim -22,000$ to $-40,000$ km s^{-1}) in GQ 1309+2904. Borguet et al. (2013) and Chamberlain et al. (2015) analyzed the rest-UV spectra of LoBALQs SDSS J1106+1939 and SDSS J0831

+0354, respectively. They found high-velocity LoBAL outflows with high energies and constrained their physical properties (~ -8000 km s^{-1} and $\sim -10{,}000$ km s^{-1}, respectively; see Section 6). Although the FeLoBALs are expected to have thick (highest log N_H) and massive outflows, potentially harboring energetic outflows, only a few FeLoBAL objects have been analyzed to determine the physical properties of their outflows (de Kool et al. 2001, 2002a, 2002b; Bautista et al. 2010; Dunn et al. 2010; Lucy et al. 2014). Because the common method (e.g., Arav et al. 2013) used to analyze BAL troughs involves individual line identification, it becomes extremely challenging to extract physical properties of an outflow that has a large number of Fe II absorption features that are blended together.

SimBAL was first introduced by Leighly et al. (2018) as a novel spectral synthesis code developed to analyze BAL outflows. Because *SimBAL* uses forward modeling with spectral synthesis, the code can be used to analyze even the most complex BAL spectroscopic features with significant line blending. The code has produced an excellent fit to SDSS J0850+4451 (Leighly et al. 2018), a LoBAL object; moreover, its sophisticated treatment of modeling the partial coverage of BAL absorbers led to further understanding of the geometry and the structure of the outflow (Leighly et al. 2019).

For thick BAL outflows, part of the radiation can be significantly absorbed by gas closer to the central engine before reaching the gas farther away, producing a phenomenon called "radiation filtering or shielding" (e.g., Leighly 2004; Leighly et al. 2007, for the case of emission lines). The question of whether or not the radiation filtering is important in outflows has gained some recent attention. Leighly et al. (2018) recently explored the possibility of radiation filtering in their *SimBAL* models and found no evidence supporting the phenomenon in SDSS J0850+4451. Miller et al. (2018) suggested a potential two-phase photoionization condition arising from radiation filtering in LBQS 1206+1052. Despite the effort to understand the radiation filtering, no definitive observational evidence has been found.

Not only do BALQs show interesting outflow signatures, they also are known to show stronger reddening and a higher scattering fraction (e.g., Sprayberry & Foltz 1992; Brotherton et al. 1997; DiPompeo et al. 2011; Krawczyk et al. 2015). Some extragalactic objects are known to show "anomalous reddening," where their reddening curves do not resemble any of the commonly used reddening curves derived from the Milky Way (e.g., Cardelli et al. 1989) or the Magellanic Clouds (e.g., Prevot et al. 1984), possibly due to a particular dust composition near the quasar (Hall et al. 2002; Leighly et al. 2009; Fynbo et al. 2013; Jiang et al. 2013; Krogager et al. 2015; Zhang et al. 2015; Meusinger et al. 2016). The nature of the strong reddening observed in BALQs may offer clues to the physical conditions and geometry of the outflows in these objects. Moreover, the dust has a significantly larger scattering cross section than the ions and can provide significant acceleration to the outflows (e.g., Fabian et al. 2008, 2018). Dusty outflows are able to harness the radiation pressure more efficiently and could potentially explain the acceleration mechanism of some of the BAL outflows with the highest velocities.

In this paper, we report the discovery of the most energetic BAL outflow analyzed to date. SDSS J135246.37+423923.5, hereafter referred to as SDSS 1352+4239, is an overlapping trough object that was initially observed by the Sloan Digital Sky Survey (SDSS). This object has all of the fascinating BAL characteristics in its spectrum, including a wide overlapping trough, anomalous reddening, and a substantial scattered light signature. With new near-infrared observations of SDSS 1352 +4239, we measured an accurate redshift, $z = 2.26$, from the Balmer emission lines. From the correct redshift, we were able to identify the fastest FeLoBAL outflow ever observed ($v \sim -38{,}000$ km s^{-1}). We performed a detailed analysis with *SimBAL* to determine the physical conditions of the outflowing cloud and constrain the energetics of the outflow. We were able to not only characterize the main BAL outflow, but we also found evidence for radiation shielding in the zero-velocity BAL system. In Section 2, we briefly reintroduce *SimBAL* and the changes that have been made since its debut in Leighly et al. (2018). In Section 3, we describe the new observation and data reduction done for SDSS 1352+4239. We introduce a general reddening curve used to model the unusual continuum shape in Section 4, and we describe the spectral model used with *SimBAL* to analyze SDSS 1352 +4239 in Section 5. We report the energetics derived from the *SimBAL* fit of the outflow in Section 6 and compare our result with other quasar objects known to have powerful outflows. Implications of our findings and a summary can be found in Sections 7 and 8.

2. *SimBAL*

Constraining the physical conditions of the outflowing clouds can be very challenging due to line blending and the non-black saturation of absorption lines from partial coverage of the emission sources. The standard method for analyzing BALQ spectra relies on the apparent optical depth (AOD) analysis (e.g., Arav et al. 2013). This method requires line identification and optical depth measurement of each absorption line. The optical depths are converted to ionic column densities and compared to the output from 1D photoionizations simulations using *Cloudy* (Ferland et al. 2017) to find the physical conditions of the gas along the line of sight. Because the AOD analysis can only provide lower limits for the column density estimates for the identified absorption lines and fails to provide accurate line ratios due to non-black saturation, accurate measurement of the density and the location of the gas with respect to the ionizing continuum source is difficult.

An alternative approach to studying BALQ spectra with the novel spectral synthesis code *SimBAL* was introduced by Leighly et al. (2018). *SimBAL* uses grids of ionic column densities calculated using the photoionization code *Cloudy* (Ferland et al. 2017) and a Bayesian model calibration method to model BALQ spectra. Because *SimBAL* employs a forward modeling technique and a sophisticated mathematical implementation of partial covering to model the absorption features (Leighly et al. 2019), it can accurately reproduce the complex absorption features in BALQSOs and constrain the physical properties of the outflow as a function of velocity. With a given set of parameters, *SimBAL* combines ionic column density information from the *Cloudy* grids, line transition strengths from atomic data and the parameterized kinematics of the outflow to create a synthetic spectrum. Additionally, the Bayesian model calibration method used in *SimBAL* yields error estimates for the physical parameters that describe the gas in the outflow. A detailed discussion on how *SimBAL* operates and a flowchart describing the relationship of the components

Table 1
Observations of SDSS J1352+4239

Observatory and Instrument	Date	Exposure (s)	Observed Frame Bandpass (Å)	Resolution
SDSS	2003 Jun 24	6300.0	3810–9189	100 km s^{-1}
Gemini (GNIRS)	2015 Feb 7	1600.0	8263–25208	240 km s^{-1}
BOSS	2016 Apr 5	8100.0	3628–10387	89 km s^{-1}
APO (Triplespec)	2018 Feb 25	5280.0	9097–24704	80 km s^{-1}

can be found in Section 3 and Figure 2 of Leighly et al. (2018), and we review the basic features here.

Each absorption component is specified by six parameters: ionization parameter log U, density log n (cm^{-3}), thickness of the gas relative to the hydrogen ionization front log N_H − log U (cm^{-2}), outflow velocity v (km s^{-1}), velocity width σ (km s^{-1}), and a covering fraction parameter log a (discussed further below). The first three parameters define the physical conditions of the outflowing gas in terms of the photoionization state, and the last three parameters define the kinematics of the gas as well as the state of non-black saturation by modeling the partial coverage using the covering fraction parameter. *SimBAL* can model a broad absorption feature with either one or multiple Gaussian opacity profiles or the "tophat accordion" model where a broad velocity profile is divided up into multiple velocity-adjacent "tophat" bins (Leighly et al. 2018). The number of bins is fixed for a given model. Each bin can have its own set of physical parameters (i.e., ionization parameter, density, and log N_H–log U) and a covering fraction parameter. Alternatively, parameters can be tied together for several velocity bins. As discussed in detail in Leighly et al. (2019), the inhomogeneous partial covering model in *SimBAL* uses a power-law distribution of opacity τ where $\tau = \tau_{max} x^a$ (Arav et al. 2005; Sabra & Hamann 2005). *SimBAL* uses log a to control the partial coverage and $x \in (0, 1)$ in the above equation is a normalized continuum source size scale. Full coverage is achieved with low values of a close to 0, and low coverage can be modeled with high values of a. Further discussion of inhomogeneous partial coverage is given in Leighly et al. (2019).

The version of *SimBAL* used in Leighly et al. (2018, 2019) used the 2013 version of *Cloudy*. After that analysis was initiated, version C17 of *Cloudy* (Ferland et al. 2017) was released, which allowed more complete and accurate photo-ionization calculations with a significantly larger atomic database. Compared to Leighly et al. (2018), the ionic column density grids that have been calculated with version C17 of *Cloudy* include the column densities of Fe II ions with a greater number of excited state levels and multiple iron-peak element ions including Co and Zn at multiple ionization states. *SimBAL* previously used a line list with 6267 transitions (78 ions; 179 counting the number of excited energy states); the updated line list includes 76488 transitions (281 ions; 997 counting the number of excited energy states). A second update from the previous version of *SimBAL* involves the grid sampling. The photoionization state of the gas changes dramatically near the hydrogen ionization front. A simple even sampling by a modest amount across the column density or the log N_H − log U parameter is insufficient to characterize the rapid change of ionic column densities across the hydrogen ionization front. For example, the ionic column densities of some species that are mostly found in the partially ionized zone such as Fe II increase by more than 4 dex as the hydrogen ionization front is traversed (e.g., Lucy et al. 2014, their Figure 10). A finer sampling is needed to properly capture the steep increase in ionic column

density around the hydrogen ionization front. However, the remainder of the hydrogen column density range does not need a finer sampling, and a grid with much finer sampling requires a tremendous amount of calculation time as well as a large file size. Therefore, we approach this problem by adopting a flexible indexing scheme where we identify the location of the hydrogen ionization front and apply the oversampling only around the region where the ionic column densities change very rapidly. In addition, the changes in physical condition before and after the hydrogen ionization front becomes more dramatic with higher ionization parameter. We took into account this change in the "sharpness" of the hydrogen ionization front when calculating the indexing scheme by increasing the grid density of the oversampled regions for higher ionization parameters (total 619,721 grid points).

A third change involves continuum modeling of the spectra. In Leighly et al. (2018), continuum-normalized spectra were used for analysis. The issue is that the depth of the absorption feature can either be overestimated or underestimated depending on the continuum placement. The new version of *SimBAL* models both the synthetic continuum model and the absorption model simultaneously, producing a full synthetic spectrum to be compared with the data as well as the unabsorbed spectrum model. Thus, *SimBAL* can fit both the emission features and the absorption features of the spectrum simultaneously to produce a more robust solution. This methodology allows more accurate measurement of the outflows. Moreover, simultaneous absorption and emission continuum modeling enables the fitting of heavily absorbed objects (e.g., overlapping trough objects) that have thick outflows and show very little residual continuum emission. In this paper, we use an emission-line template developed from an *HST* observation of Mrk 493 (Section 4.3). More generally, we use principal component analysis (PCA) eigenvectors for the continuum modeling with *SimBAL* (H. Choi et al. 2020, in preparation).

3. Observations and Analysis

The observations of SDSS 1352+4239 discussed in this paper are listed in Table 1.

3.1. Gemini GNIRS Observation

SDSS 1352+4239 was observed using GNIRS[8] on the Gillett Gemini (North) Telescope using a standard cross-dispersed mode (the SXD camera with the 31.7 l/mm grating) and a 0.″45 slit. Eight 200 s exposures were made on 2015 February 7 in an ABBA dither pattern. Four 1 s exposures were made of the A0 star HIP 61471 at a similar airmass for telluric correction. The data were reduced using the IRAF *Gemini* package, coupled with the GNIRS XD reduction scripts, in the standard manner for near-infrared spectra, through the spectral extraction step. For telluric correction, the *Gemini* spectra of
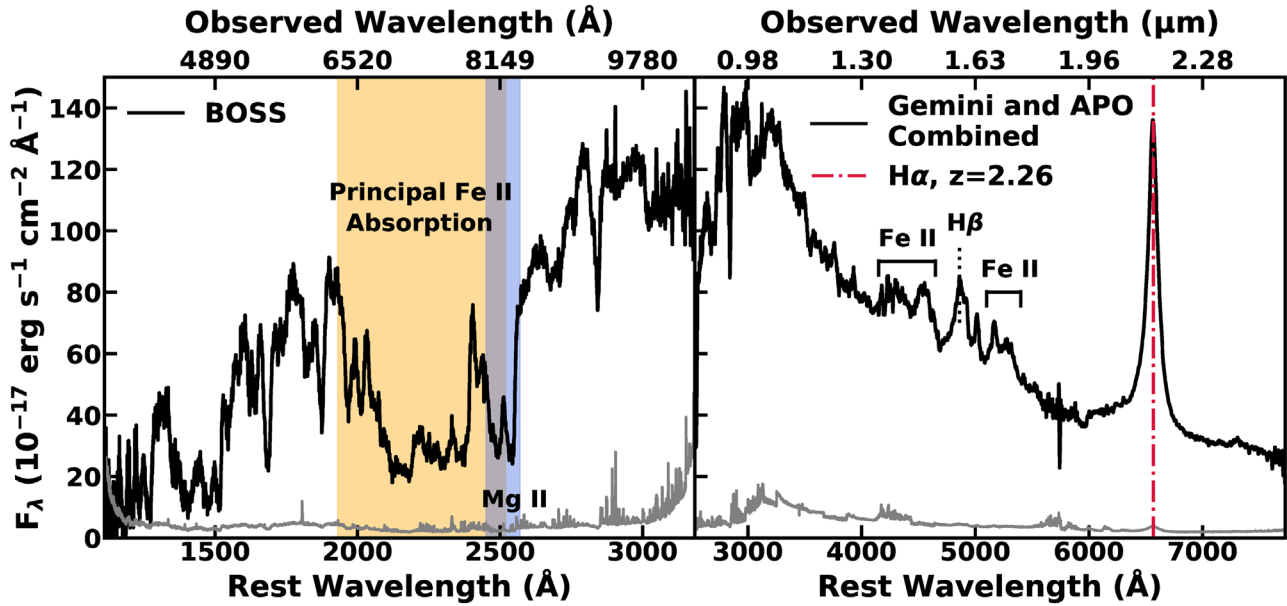
---

[8]　http://www.gemini.edu/sciops/instruments/gnirs

Figure 1. The BOSS spectrum on the left shows an "overlapping trough" feature from the Fe II absorption lines. The main iron trough and Mg II absorption features are marked on the left panel. BOSS spectrum showed no strong emission features that could be used to estimate the redshift. Therefore, we used Hα in the combined GNIRS+APO spectrum (right) to measure the redshift for SDSS J1352+4239. The flux level for the Gemini and APO combined spectrum has been corrected to match BOSS flux density. The gray lines below the spectra show the uncertainties associated with the data.

the source and the telluric standard star were converted to a format that resembled IRTF SpeX data sufficiently that the Spextool xtellcor package (Vacca et al. 2003; Cushing et al. 2004) could be used.

3.2. APO Triplespec Observation

SDSS J1352+4239 was observed using Triplespec[9] (Wilson et al. 2004) on the Apache Point Observatory Astrophysical Research Consortium 3.5 m telescope on 2018 February 25 under photometric conditions. The 240 s observations were made in a standard ABBA dither pattern and split into two segments of 10 and 12 exposures. Twenty 20 s exposures of the A0 star HIP 61471 were made before the first segment, and twelve 20 s exposures of the A0 star HIP 71172 were made after the second segment. The 1″1 slit was used. The resolution was measured using the night sky lines to be 80 km s^{-1} near 1.5 μm.

The spectra were extracted in a standard manner using TripleSpecTool, a modification of SpexTool (Vacca et al. 2003; Cushing et al. 2004). TripleSpecTool uses the airglow emission lines for wavelength calibration. To account for a very small amount of flexure, wavelength calibration solutions were computed for each AB dither pair sequence of exposures. The telluric correction was performed using the adjacent observation of the A0 star (Vacca et al. 2003).

The spectra were combined with the Gemini spectrum using a flux-weighted average, where the variance was based on the deviations of the spectrum around a best-fitting linear model to 21 pixel bins, after first down-sampling the APO spectra to the Gemini resolution. The combined spectrum is shown in the right panel of Figure 1.

3.3. The SDSS and BOSS Observations and Merging the Spectra

SDSS J1352+4239 was observed by SDSS and by the Baryon Oscillation Spectroscopic Survey (BOSS) program. We did not find any measurable flux offset or any strong evidence for spectral variability in the two spectra. We chose to use the BOSS optical data from the SDSS archive because the data were taken closer to our near-infrared observations, and the spectrum provides larger wavelength range coverage than the SDSS spectrum. The BOSS and combined near-infrared Gemini and APO spectra are shown in Figure 1. We used the flux density of BOSS spectrum and the wavelength range between rest frame ~3000 to ~3100 Å to match and merge the optical BOSS and near-infrared Gemini and APO spectra.

3.4. The Redshift

SDSS 1352+4239 was first cataloged in the SDSS Third Data Release catalog (Schneider et al. 2005), where the redshift was listed as 2.0385. Other published redshifts range from 2.000 (Meusinger et al. 2012) to 2.049184 (Hewett & Wild 2010). The difficulty in estimating the redshift occurs because there are no strong emission lines in the SDSS spectrum. A broad bump just longward of the Mg II absorption was identified as Mg II emission by Trump et al. (2006, their Figure 10). On the other hand, the redshift of the absorption features is fairly obvious ($z = 1.954$), based on the characteristic pattern of Mg II and Fe II absorption lines (e.g., Lucy et al. 2014, Figure 12).

The redshift of SDSS 1352+4239 can be measured unambiguously from the infrared spectrum. We use Hα because there are no prominent [O III] lines, and Hβ is blended with Fe II emission. The line appears slightly asymmetric due to Fe II emission, so we fit it with two Lorentzian profiles. The peak of the narrower one yields a redshift of 2.2639 ± 0.0008, ~11% larger than any of the previous estimated values,
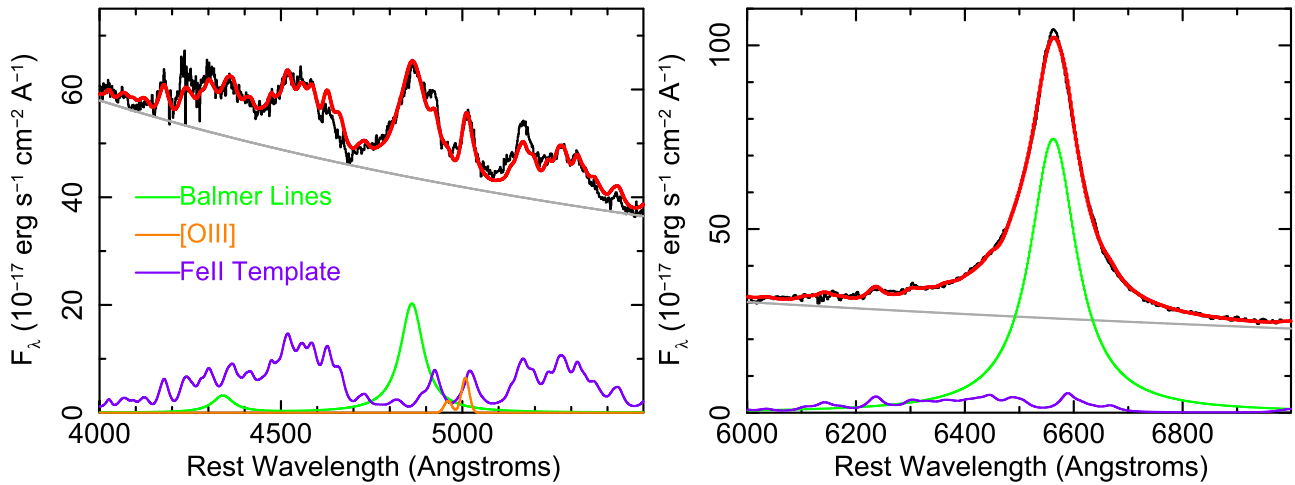
Figure 2. The model fits to the combined Gemini and APO spectrum. The left panel shows the bandpass that includes Hβ, and the right panel shows the bandpass that includes Hα. The strong Fe II emission obscures the Hβ line, so the two regions of the spectrum were fitted simultaneously, requiring the FWHM of the Balmer lines to be equal.

implying that the outflow has a much larger velocity than previously suspected.

3.5. The Black Hole Mass

We estimated the black hole mass using the Hβ emission line. Strong Fe II emission is apparent throughout the rest-frame optical spectrum, and especially around Hβ. We constrain the shape of Hβ by simultaneously fitting Lorenzian profiles to each of Hα, Hβ, and Hγ, and constraining their widths to be the same and their relative central wavelengths based on known wavelengths of these lines. We used Sherpa for spectral fitting[10] (Freeman et al. 2001). The strong Fe II emission was modeled using the catalog of Fe II emission lines obtained from I Zw 1 (Véron-Cetty et al. 2004). No obvious [O III] lines are visible in the spectrum, but they are included with a fixed width of 1500 km s^{-1} and variable position and flux, with the 4960 Å component constrained to have the same width and fixed relative flux with respect to the 5008 Å component. The best-fitting model is shown in Figure 2.

To determine the radius of the broad-line region, we refer to Bentz et al. (2013), who find that $\log(R_{BLR}) = K + \alpha \log[\lambda L_\lambda(5100)/10^{44} \text{ erg s}^{-1}]$. The continuum flux density at 5100 Å was estimated from the combined Gemini and APO spectrum to be $F_{5100} = 48.71 \times 10^{-17}$ erg s^{-1} cm^{-2}Å^{-1}. With the cosmological parameters used by Bentz et al. (2013; $H_0 = 72$ km s^{-1} Mpc^{-1}, $\Omega_M = 0.27$, and $\Omega_\Lambda = 0.73$), we obtain a luminosity distance $D_L = 18074$ Mpc. Using $K = 1.527^{+0.031}_{-0.031}$ and $\alpha = 0.533^{+0.035}_{-0.033}$, we obtain an estimate of the radius of the Hβ emitting broad-line region of 1315^{+480}_{-340} lt-day corresponding to $1.1^{+0.4}_{-0.3}$ parsec. For reference, we also calculated the location of the C IV emitting region using the equation given by Lira et al. (2018, Equation (1)). We estimated the continuum flux density at 1345 Å to be $F_{1345} = 343.2 \times 10^{-17}$ erg s^{-1} cm^{-2}Å^{-1} after scaling the composite SED (Richards et al. 2006a) to match the near-infrared (rest-optical) photometry (Section 4.1) and calculated the location of the C IV emitting region of 199^{+436}_{-150} lt-day or $0.17^{+0.37}_{-0.13}$ parsec.

The model fit yields an FWHM of the Balmer lines of 4720 km s^{-1} for a Lorentzian profile. We estimate the black hole

mass in the usual way. We refer to Collin et al. (2006), who provide line-shape-based correction factors based on the ratio of the FWHM to σ_{line}, where σ_{line} is the line dispersion. For a Lorentzian profile, FWHM/$\sigma_{\text{line}} \Rightarrow 0$, and therefore $f = 1.5$. We estimate that the black hole mass is $8.6 \times 10^9 M_\odot$.

4. Continuum Modeling and Spectral Energy Distribution

4.1. The Long-wavelength Spectrum

SDSS J1352+4239 shows a peculiar continuum shape compared to a typical quasar spectrum. We used the composite quasar SED from Richards et al. (2006a) and the composite spectrum from Francis et al. (1991) to analyze the shape of the underlying AGN continuum of the object using both the spectrum and the photometry from SDSS, 2MASS, and *Wide-field Infrared Survey Explorer* (*WISE*; Figure 3). In Figure 3, compared with the composite spectrum (Francis et al. 1991), the spectrum of SDSS J1352+4239 is similar to a typical unreddened quasar at wavelengths longward of $\sim$3000 Å. In the infrared region, the shape of the SED of SDSS J1352 +4239 also resembles the mean quasar mid-infrared SED shape. Because the continuum bluewards of the break shows a large difference in the slope, we analyzed the reddening and the slope of the continuum in the long-wavelength region separately from the short-wavelength region.

Krawczyk et al. (2015) found that BAL quasars are redder than the non-BAL quasars, and that the SMC reddening curve (extinction curve derived from the Small Magellanic Cloud) fits BAL quasars well in most cases. Therefore, we used the SMC reddening law to measure the reddening in SDSS J1352+4239. We used the Markov Chain Monte Carlo code emcee[11] (Foreman-Mackey et al. 2013) to fit the SMC (Prevot et al. 1984) reddened composite SED to the rest-frame optical/near-infrared photometry points and found no evidence for reddening in the optical/near-infrared region of the spectrum ($E(B - V) < 0.002$).

We also fit the optical/near-infrared part of the continuum using an SMC-reddened power law to get an estimate of the slope and reddening. We measured a power-law slope of $-1.82(\pm 0.02)$, consistent with a mean spectral slope value for
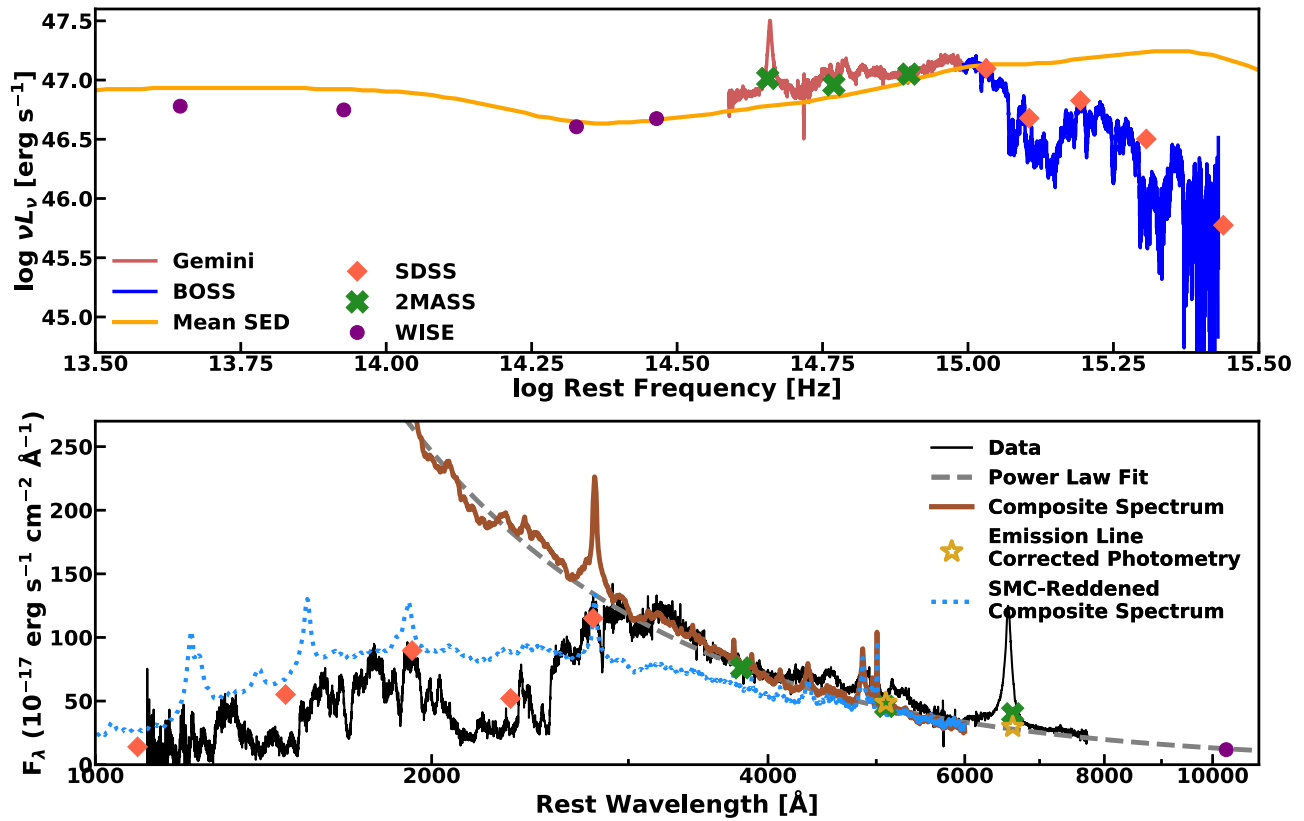

Figure 3. SDSS J1352+4239 is plotted with the mean SED from Richards et al. (2006a) in the upper panel. The lower panel shows the power-law continuum fit to long wavelengths ($\lambda > 3000$ Å) and the composite spectrum from Francis et al. (1991). The H and K band photometry points have been corrected for the hydrogen line emission and iron emission using 2MASS filter functions (Cohen et al. 2003) and iron emission templates created from the decomposition of the I Zw 1 spectrum (Véron-Cetty et al. 2004). The SMC-reddened composite spectrum with $E(B - V) = 0.17$, plotted in dotted blue in the lower panel, demonstrates that the SMC reddening curve fails to reproduce the continuum shape of SDSS 1352+4239. While the observed and composite continuum shapes are similar longward of ∼3000 Å, SDSS 1352+4239 diverges significantly at shorter wavelengths. Because of the dramatic change in the SDSS 1352+4239 continuum shape at ∼3000 Å , we use a nontraditional reddening curve to model the continuum emission (Section 4.2).

BALQs (−1.83, Krawczyk et al. 2015), and no reddening ($E(B - V) < 0.03$) for the continuum from 1.4 μm to 3788 Å. Thus, the object has a typical value of spectral slope and no evidence for reddening in the long-wavelength region, despite significant reddening at shorter wavelengths.

To estimate the bolometric luminosity, we used the bolometric correction factor (BC) from Gallagher et al. (2007) who provide bolometric corrections for monochromatic luminosity at two different wavelengths. The strong reddening in the spectrum is only seen at wavelengths shortward of ∼3000 Å. Therefore, we used the monochromatic luminosity at 5100 Å of SDSS J1352+4239 (Section 3.5) and obtained the log bolometric luminosity of 48.0 ± 0.2 (erg s^{-1}), with the uncertainties estimated from the uncertainties associated with the bolometric correction factor (BC = 10.47 ± 4.14).

SDSS J1352+4239 is among the most luminous quasars observed, and it is considered a hyper-luminous quasar (i.e., quasars with $L_{\rm Bol} > 10^{47}$ erg s^{-1}). The bolometric luminosity of SDSS J1352+4239 is comparable to the objects in the WISSH quasar sample (Bischetti et al. 2017) where they focused on a sample of *WISE*/SDSS selected hyper-luminous quasars to study the power and the effect of the AGN feedback. The mass accretion calculated from the bolometric luminosity, assuming the energy conversion efficiency (η) of 0.1, is 176 $M_\odot$ per year. Compared with the black hole mass of 8.6×10^9 $M_\odot$, SDSS J1352+4239 is radiating at about 93% of the Eddington limit.

4.2. Anomalous Reddening

As can be seen from Figure 3, the shape of the continuum for SDSS J1352+4239 is quite peculiar, but it is not unprecedented. Among other BAL objects with anomalous reddening, Mrk 231 shows steep reddening in the near-UV to optical part of the continuum (e.g., Smith et al. 1995; Veilleux et al. 2013). Leighly et al. (2014) fit the continuum in Mrk 231 and concluded that a Type Ia supernovae reddening curve (Goobar 2008) best describes the reddening behavior of Mrk 231. Jiang et al. (2013) derived a reddening curve from IRAS 14026+4341 by comparing the object to a quasar composite spectrum and found that their reddening curve could be explained by a particular distribution of dust grain sizes (one lacking large grains, $a_{\rm max} = 70$ nm). However, in the case of WPVS 007 (Leighly et al. 2009), no particular grain distribution was able to model their anomalous reddening curve.

We tried using the reddening templates developed with WPVS 007 (Leighly et al. 2009) and IRAS 14026+4341 (Jiang et al. 2013) as well as the reddening model used for Mrk 231 (Leighly et al. 2014) to model the break in the continuum shape. However, none of the anomalous reddening models were able to appropriately model the continuum shape of SDSS J1352+4239, because their slopes and the locations of sharp reddening increase did not match the continuum shape of SDSS J1352+4239.

Therefore, we developed a general anomalous reddening curve. Using the general reddening equation A(λ) =
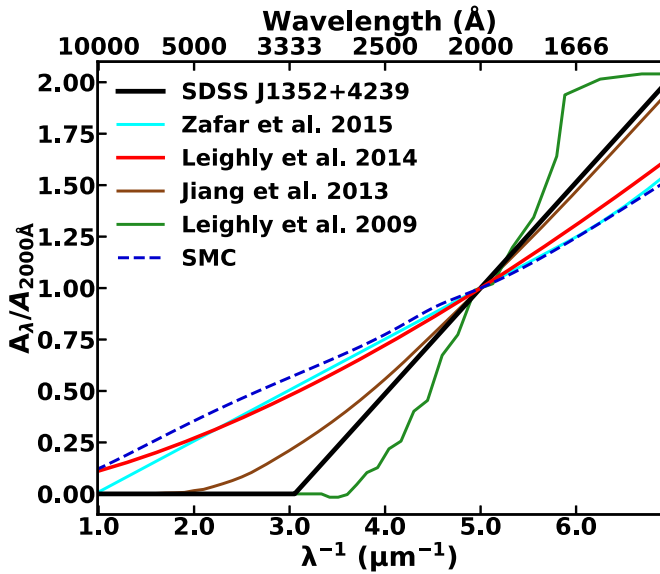
Figure 4. The reddening curve for SDSS J1352+4239 found from *SimBAL* fits using our model ($p = 0.57 \pm 0.003$, $\lambda_{Break} = 0.328 \pm 0.001$ (μm)) compared with other reddening curves developed for anomalous reddening. The reddening curves have been normalized to A_λ at 2000 Å. Anomalous reddening curves by Leighly et al. (2009) and Jiang et al. (2013) show different break wavelengths and slopes. The SMC reddening curve and an empirical reddening curve derived from a sample of reddened quasars by Zafar et al. (2015) is also plotted ($A_V = 0.51$) for comparison.

$2.5 \log\{C(\lambda)/S(\lambda)\}$ where $S(\lambda)$ is the reddened spectrum and $C(\lambda)$ is the intrinsic spectrum, our general reddening curve has the form of a power law.

$$A(\lambda(\mu m)) = \begin{cases} p\left(\dfrac{1}{\lambda} - \dfrac{1}{\lambda_{Break}}\right), (p > 0) & \text{if } \lambda \leqslant \lambda_{Break} \\ 0 & \text{if } \lambda > \lambda_{Break}. \end{cases}$$

Our anomalous reddening curve generates reddening from a specified wavelength (λ_{Break}) to shorter wavelengths with $A(\lambda)$ gradually increasing from zero, and therefore, there is no reddening at long-wavelength region as required. The reddening equation requires two parameters: the slope of the curve (p) and a reddening starting wavelength (λ_{Break}). Figure 4 illustrates various reddening curves. Our general reddening model provides excellent fits for other anomalously reddened BALQ spectra as well (H. Choi et al. 2020, in preparation).

To fit the shorter wavelength spectrum, we fixed the power-law spectral slope to the value we found from the optical/near-infrared photometry fit, and only varied the two anomalous reddening parameters and the power-law normalization to model the continuum with *SimBAL*.

4.3. Modeling the Line Emission

Visual inspection of SDSS J1352+4239 revealed that the object potentially has a weaker Mg II emission and stronger iron emission compared with the typical AGN spectrum. It is not possible to model the individual emission lines due to the heavy absorption features seen throughout the bandpass. Instead, we constructed a set of broadband emission templates to model the emission lines. It is well known that the ratio between the strengths of the prominent emission lines (e.g., Mg II, C IV) and the strength of the iron emission differs from object to object (e.g., Sulentic et al. 2000).

Therefore, we created separate emission-line templates for the iron emission and several other emission-line templates for other emission lines so that our model can create the iron emission independently from other emission lines. Mrk 493 is a narrow-line Seyfert with a strong Fe II emission, making it a suitable target for AGN emission-line analysis. It was observed by *Hubble Space Telescope*[12] to create a high-resolution and good signal-to-noise ratio Fe II template. From this Mrk 493 spectrum, we derived empirical emission templates for the iron emission (the Fe II pseudo-continuum) and for other emission lines (e.g., Lyα, Si IV, C IV, C III], Mg II, Balmer lines) separately and used the extracted templates to model the emission features of SDSS J1352+4239.

In order to separate the Fe II emission from the other emission lines in the Mrk 493 spectrum, we used Sherpa to model the spectrum using a power law, existing Fe II templates (Véron-Cetty et al. 2004: 4000 Å $\lesssim \lambda_{rest} \lesssim$ 7000 Å, Leighly & Moore 2006: 2000 Å $\lesssim \lambda_{rest} \lesssim$ 3000 Å and Leighly et al. 2011: 3000 Å $\lesssim \lambda_{rest} \lesssim$ 4000 Å) and Gaussian line profiles for all other emission lines present in the spectrum. We then subtracted the Mrk 493 spectrum by the emission-line models consisting of only the non-Fe II emission lines and power-law continuum to obtain the Fe II emission templates. Separate emission templates for other major emission lines were made from the non-Fe II emission-line component of the same model. We merged the resulting Fe II emission templates together to create a single broadband emission template (1500 Å $\lesssim \lambda \lesssim$ 7500 Å). We did not attempt to do the same for the non-Fe II emission-line templates to allow *SimBAL* more flexibility in fitting the major emission-line features so that each template can be scaled to its own independent normalization coefficient. The final emission-line templates consist of a single full wavelength range template for Fe II emission lines and four emission templates divided in wavelength sections mentioned above for the non-Fe II AGN emission lines.

5. Best-fitting Model

We created a complex spectral model for SDSS J1352+4239 to extract the physical properties of the outflow. Our best-fitting model is made of four major components including two absorbing components. The continuum and line emission were modeled by a power law and emission-line templates described in Section 4.3. A scattered non-absorbed continuum emission component was added to the model to produce the peculiar non-black saturation shape under the iron trough. Reddening was applied to all components using the anomalous reddening model discussed in Section 4.2. We first discuss the main blueshifted absorption-line component in Section 5.1, then explore the necessity of the scattered light component in Section 5.2 and a zero-velocity absorption component in Section 5.3. The results are summarized in Table 2.

The model is given by:

$$f_{model} = \text{Reddening} \times \{(f_{Continuum} + f_{LineEmission}) \\ \times I_{High-Velocity} \times I_{Zero-Velocity} + f_{Scattered\,Flux}\}$$

where $f(\lambda)$ is the flux from each component and the final model and $I(\lambda)$ is the normalized flux (I/I_0) from each absorption component. Figure 5 shows the best-fit model of SDSS J1352+4239.

---

[12] PI: Park, "A Definitive UV−Optical Template for Iron Emission in Active Galactic Nuclei," program number 14744.
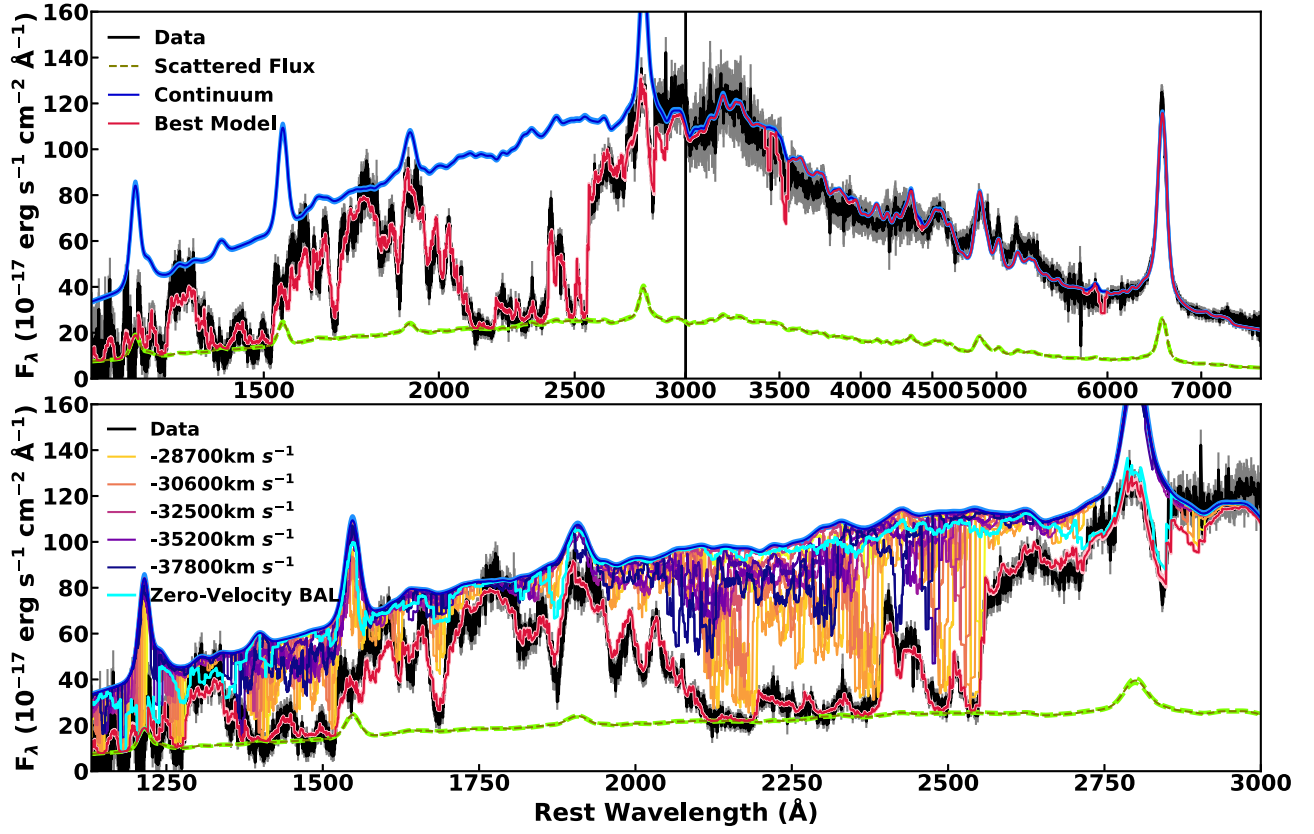
Figure 5. Upper panel: our best-fitting model described in Section 5. Lower panel: decomposition of 10 tophat bins is shown in different colors (from yellow to navy); the zero-velocity BAL component is plotted in cyan. The velocities of five of the ten tophat bins for the main complex are labeled on the figure. Each bin in the absorption complex creates an absorption feature at a different velocity. The combination of 10 bins create the full trough, and we harvest the information about the physical parameters of the outflow as a function of velocity.

Table 2
Physical Parameters and Derived Outflow Properties from the Best-fitting *SimBAL* Model

Outflow Properties	Higher-velocity Group	Lower-velocity Group	High-velocity Total[a]	Zero-velocity Component
		Physical Parameters		
$v_{outflow}$ (km s^{-1})[b]	$-38,000$ to $-33,000$	$-33,000$ to $-28,000$	$-38,000$ to $-28,000$	-8900 to 6700
$\log U$	$0.82^{+0.07}_{-0.12}$	$-0.56^{+0.07}_{-0.08}$	...	-2.8 to 1.8[b]
$\log n$ (cm^{-3})	$6.12^{+0.12}_{-0.07}$	$7.43^{+0.09}_{-0.07}$	...	<5.0[e]
$\log N_H - \log U$ (cm^{-2})[b]	23.0–23.16	23.13–23.17	...	21.9–23.0
$\log a$[b,c]	0.91–1.9	0.38–1.13	...	-0.58 to 1.92
		Derived Outflow Properties		
$\log N_H$ (cm^{-2}), per bin[b,c]	22.03–22.85	21.41–22.06	...	18.31–21.82
$\log N_H$ (cm^{-2}), total[d]	$23.11^{+0.07}_{-0.06}$	$22.57^{+0.06}_{-0.07}$	23.22 ± 0.05	$21.85^{+0.05}_{-0.06}$
$\log R$ (pc)	$0.97^{+0.05}_{-0.04}$	1.0 ± 0.02	0.93–1.02	>1.0[e]
$\log \dot{M}$ ($M_\odot$ yr^{-1})[f]	$3.41^{+0.04}_{-0.05}$	$2.81^{+0.06}_{-0.07}$	3.51 ± 0.04	...
$\log \dot{P}$ (dyne)[f]	$38.77^{+0.04}_{-0.05}$	$38.08^{+0.06}_{-0.07}$	38.85 ± 0.04	...
$\log L_{KE}$ (erg s^{-1})[f]	$48.04^{+0.04}_{-0.05}$	$47.25^{+0.06}_{-0.07}$	48.1 ± 0.04	...

Notes.
[a] The values are the combined result of the left two columns.
[b] The range of values estimated from the multiple bins is reported.
[c] Large value of $\log a$ corresponds to small covering fraction
[d] Covering fraction weighted values are reported (Section 5.1).
[e] Zero-velocity component is located at a larger distance than the main high-velocity component (Section 7.1).
[f] The global covering fraction $\Omega = 0.2$ was used (e.g., Hewett & Foltz 2003), and further discussion of Ω can be found in Section 6.

Depending on the geometry and the angular size scale of the BAL outflowing cloud, the covering fraction for the accretion disk and the line-emitting gas (broad-line region, BLR) can be different. Leighly et al. (2019) demonstrated how *SimBAL* can be used to test the scenarios where the outflowing cloud has multiple covering fractions for different AGN components. We tested both two-covering models where the covering fraction parameters for the line emission and the continuum emission were allowed to differ, and we tested single-covering models. We concluded that there is no strong evidence for a different covering fraction for emission lines and continuum emission in SDSS J1352+4239. Therefore, we used a model with a single-covering fraction for both emission components.

The tophat accordion model provided an exceptional fit of the complex velocity structures of the trough in SDSS J1352+4239, and yielded the physical parameters of the outflows as a function of velocity (Figure 6). We fit the high-velocity troughs with a 10-bin tophat model with an additional 7-bin tophat model for the zero-velocity absorption feature we identify near the Mg II emission lines (Section 5.3). Leighly et al. (2018) explored the dependence on number of bins and concluded that the number of bins does not change the result of the fit except when too few bins were used, and that there were no significant differences between the results obtained with models with different number of bins. We experimented with 7-, 10-, and 15-bin tophat accordion models and found that 10 bins were sufficient to model the complex. Ten bins span a velocity range from $\sim -38{,}000\ \mathrm{km\ s^{-1}}$ to $\sim -28{,}000\ \mathrm{km\ s^{-1}}$ with the total velocity width of $\sim 10{,}000\ \mathrm{km\ s^{-1}}$ (Figure 5).

The physical parameters and the derived outflow properties for the high-velocity trough and zero-velocity component (Section 5.3), as well as for each group, are reported in Table 2. The main blueshifted trough in SDSS J1352+4239 was modeled with a 10-bin tophat accordion model where the bins were divided into two groups with a single ionization parameter and density for all bins in each group as described in Section 5.1. The values for $\log U$, $\log n\ (\mathrm{cm^{-3}})$, $\log N_{\mathrm{H}} - \log U\ (\mathrm{cm^{-2}})$, and $\log a$ were directly taken from the the physical fit parameters of the best-fitting model. The hydrogen column density values that have been corrected for the partial coverage with $\log a$ and the outflow properties (e.g., $\log \dot{M}$, $\log L_{\mathrm{KE}}$) have been calculated from the aforementioned fit parameters. For $\log N_{\mathrm{H}} - \log U\ (\mathrm{cm^{-2}})$, $\log a$, and $\log N_{\mathrm{H}}\ (\mathrm{cm^{-2}})$, the ranges reflect the values we found for the individual bins. Total $\log N_{\mathrm{H}}$ for the groups are also reported. Uncertainties for each parameter were calculated from the posterior probability distributions of the MCMC chain. We did not attempt to model the posterior distribution (e.g., Gaussian distribution); instead, we calculated the median, 1σ, 2σ, and 3σ values directly from the posteriors. The uncertainties reported in the Table 2 represents 95% confidence regions. A global covering fraction (Ω) of 0.2 was used for the calculations and further discussion of this parameter can be found in Section 6.

5.1. The High-velocity Component

The 10 bins for the main high-velocity trough were grouped into two sets with each group having a single density and ionization parameter. Our initial investigation with *SimBAL* models revealed that the bins at higher velocities and at lower velocities have clear differences in their physical parameters, primarily in their densities. Subsequently, we found that the two density groups also had different characteristic ionization
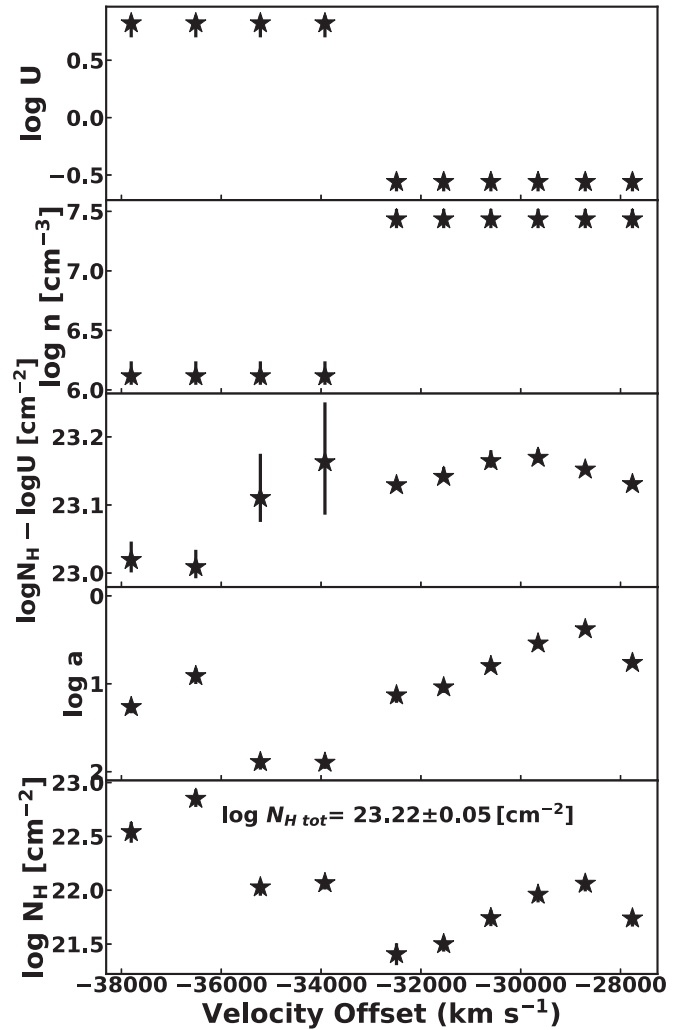

Figure 6. Physical parameters as a function of velocity with error bars representing 95% confidence regions. The parameters plotted in the top four panels were directly fitted with *SimBAL*. In the bottom panel, the hydrogen column density values (log N_{H}), corrected for the covering fraction from each bin, were calculated from log U, log N_{H} − log U, and log a. The total log N_{H} value for the outflow, calculated by adding the hydrogen column density values from all 10 bins, is also reported in the bottom panel. The two groups ($-38{,}000 \sim -33{,}000\ \mathrm{km\ s^{-1}}$ and $-33{,}000 \sim -28{,}000\ \mathrm{km\ s^{-1}}$) are constrained to each have the same density and ionization parameter (top two panels), while the log N_{H}–log U parameter and the covering fraction parameter (lower log a values indicate higher covering fraction) were allowed to vary independently for each bin. The highest covering fraction (lowest log a value) occurs around $\sim -30{,}000\ \mathrm{km\ s^{-1}}$ and the column density parameter log N_{H}–log U also peaks around the same velocity. This shows that most of the opacity is generated near this velocity (see also Figure 7).

parameters. Therefore, we assigned a single ionization parameter and density to each group.

Fe II has a plethora of excited state levels, ranging from low-level excited states (0–0.12 eV) as well as high levels (>2.89 eV), making the strengths of the excited state Fe II lines very density sensitive (e.g., Lucy et al. 2014). Fe II ions are populated deep in the photoionized cloud away from the incoming radiation, because the ionization potentials to create Fe II ions is relatively low (7.9 eV). Therefore, Fe II ions require a large column density to be significant (column density reaching beyond hydrogen ionization front); otherwise, most of the iron atoms will be in a higher ionization state than Fe II. Thus, the presence of the excited state Fe II lines along with other low-ionization lines (e.g., Mg II)
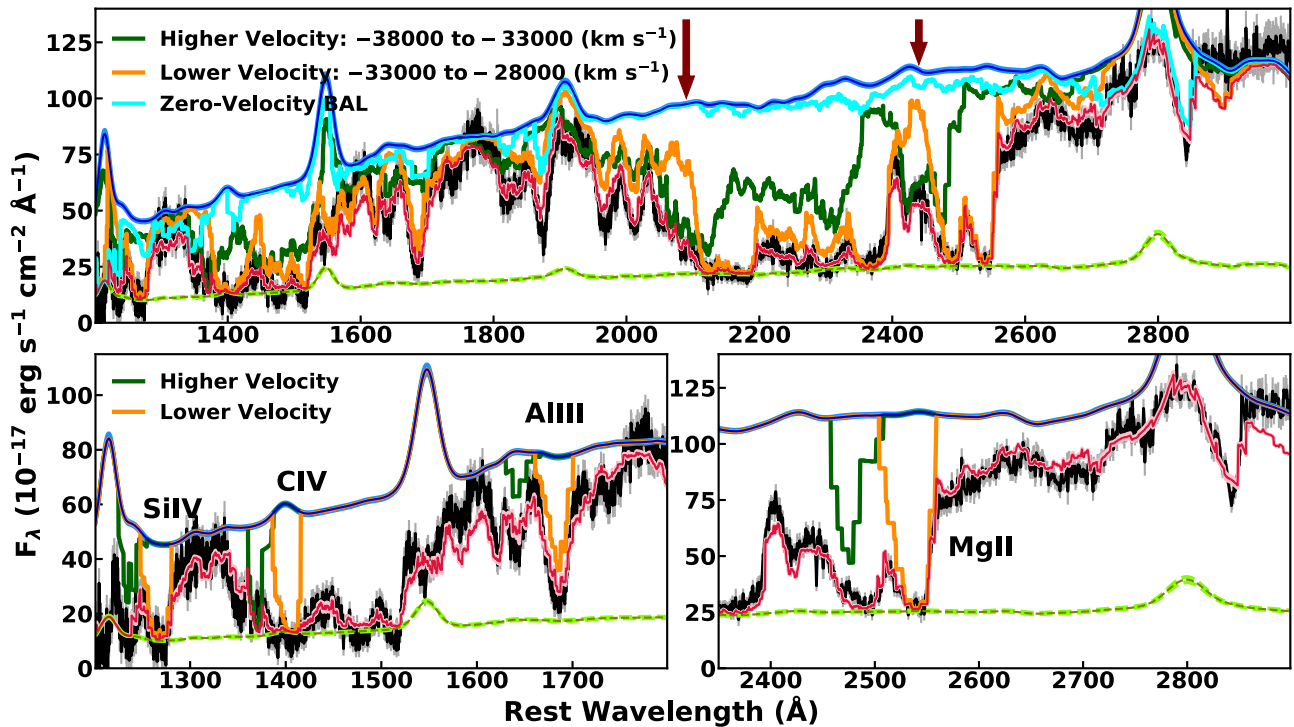
Figure 7. The top panel shows the two models generated from combining only the higher- and lower-velocity bins in dark green and orange, respectively. The regions where the higher-velocity group plays a significant role in producing sufficient opacity to model the trough are marked with arrows in the top panel. The bottom two panels show how some of the common BAL absorption lines (Si IV, C IV, Al III, Mg II) have been modeled by the higher-velocity group and the lower-velocity group. The best-fitting model, continuum, and the scattered flux component are plotted in same colors as Figure 5.

helps *SimBAL* to constrain both the density and the thickness of the outflowing gas. We see in Figure 5 not only how all 10 bins model the trough together in combination but also how each tophat bin creates a large number of absorption lines. Together, the physical parameters at each velocity can be constrained.

Figure 6 shows the outflow physical parameters as a function of velocity. We found the high-velocity part of the outflow has lower density ($\log n \sim 6.12$ (cm^{-3})) and higher ionization ($\log U \sim 0.82$) than the lower-velocity group ($\log n \sim 7.43$ (cm^{-3}), $\log U \sim -0.56$). The large combination parameter ($\log N_{\rm H}$–$\log U$) of ~ 23.1 (cm^{-2}) reflects the significant opacity from Fe II ions that we see in the data. The covering fraction parameter ($\log a$) changes strongly with velocity, and the bottom panel in Figure 7 shows how the shape of the opacity profile of the absorber closely follows the shape of $\log a$. Moreover, the large covering fraction (low $\log a$) and high $\log N_{\rm H}$–$\log U$ parameter found near $\sim -29,000$ km s^{-1} indicate that a large amount of opacity is concentrated around that velocity region in the outflow. Similarly, Leighly et al. (2018) also found a "concentration" region in their *SimBAL* model of SDSS J0850+4451, i.e., an enhancement in column density for a few of the bins in their 11-bin tophat model. By summing the hydrogen column density values weighted by the covering fraction from all 10 bins, each calculated from the $\log U$ parameter, $\log N_{\rm H}$–$\log U$ parameter, and covering fraction parameter ($\log a$) per bin ($\log N_{\rm H} = (\log N_{\rm H} - \log U) + \log U - \log(1 + 10^{\log a})$ Arav et al. 2005; Leighly et al. 2018, 2019), we estimated a covering fraction weighted total hydrogen column density of $\log N_{\rm H} = 23.22 \pm 0.05$ (cm^{-2}) (95% confidence errors, bottom panel in Figure 6).

Figure 7 shows how the two tophat groups model the wide absorption feature. The higher-velocity component contributes less opacity than the lower-velocity component; however, the lower-velocity component alone cannot produce the wide trough we see in the data. The lower-velocity component has gaps between ~ 2450 Å and ~ 2600 Å, and near ~ 2100 Å where the Fe II and other iron-peak ions in the high-excited states are expected to be the main source of the opacity. The problem is that the lower-velocity component cannot produce enough opacity in those regions without creating a deep absorption feature near ~ 2600 Å that is not present in the spectrum. Therefore, the higher-velocity group (with distinct values for the density and ionization parameter) was needed to fill in the gaps in the trough where the lower-velocity component did not produce enough opacity to complete the absorption feature (arrows in Figure 7).

In Figure 7, we also see that the concentration of opacity and strong absorption contribution from the lower-velocity component, as expected from Figure 6, and the shape of the absorption profile for an individual transition (dark green and orange lines in the lower panel) closely follows the shape of the covering fraction parameter. The blended lines in the main trough are nearly saturated even with the partial covering; the flux at the bottom of the trough is mainly modeled by the scattered light component.

5.2. The Scattered Light Component

SDSS J1352+4239 shows an extreme case of non-black saturation in the main trough where the emission at the bottom of the trough increases as a function of wavelength and contains a significant amount of flux. Non-black saturation of BAL features is very common and is thought to originate from the BAL outflow not entirely covering the continuum sources, which includes the accretion disk continuum and broad emission-line features (e.g., Barlow & Sargent 1997). Continuum scattering is
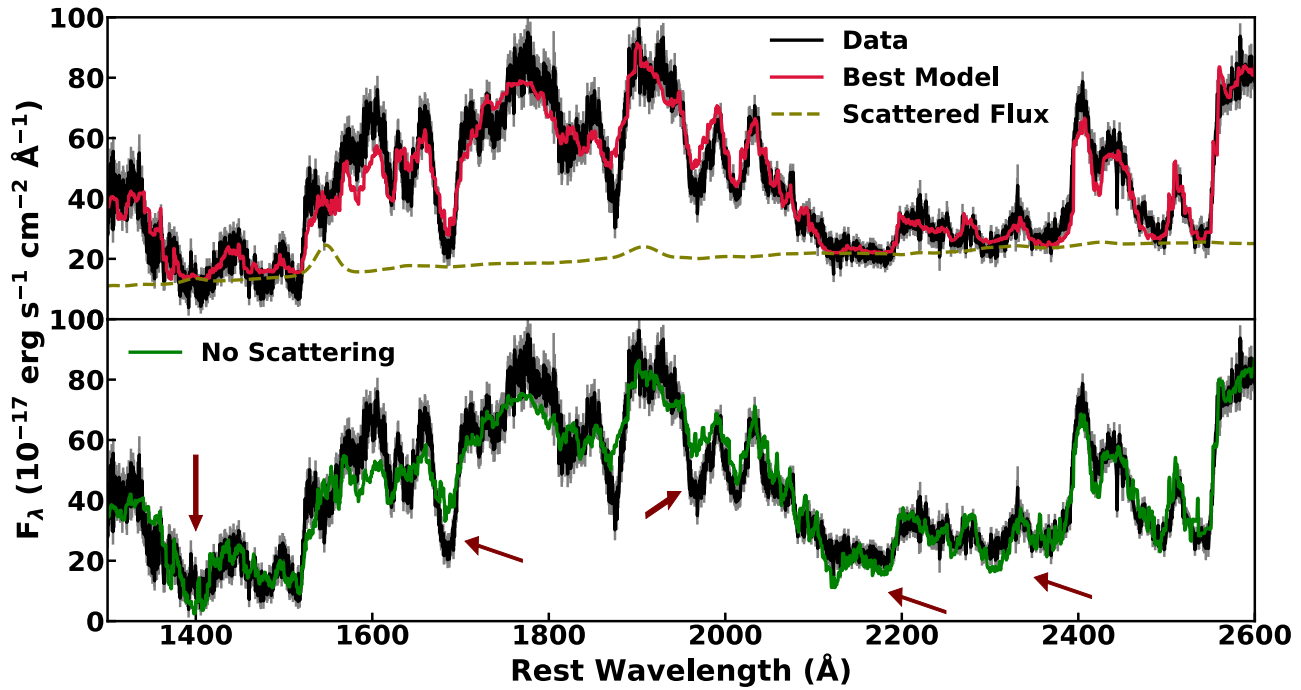
Figure 8. The top panel shows the data and the best-fit model that has the scattered flux component in it. The bottom panel shows a model that does not have the scattered light component. The scattered light component is clearly necessary to create an appropriate trough shape.

not uncommon in BALQs, and it is known from spectropolarimetry that frequently the troughs are highly polarized, indicating an origin in scattered light (e.g., Cohen et al. 1995; Ogle et al. 1999). The shape of the offset found under the trough in SDSS J1352+4239 suggests that this component is scattered light from the accretion disk continuum and line emission with the wavelength dependence created by the reddening. We modeled the scattered light component by multiplying the scattering fraction parameter by the emission model, which consists of the sum of the reddened power-law continuum and line emission, and we added this component to the absorbed emission model:

$$f_{\text{Scattered Flux}}(\lambda) = (f_{\text{Continuum}}(\lambda) + f_{\text{LineEmission}}(\lambda)) \\ \times \text{Scattering Fraction.}$$

The reddening of the scattered flux is assumed to be the same as the continuum reddening, and we assume that the scattered light is not absorbed by the wind. Our best model creates the underlying emission feature with a scattering fraction of $\sim 29\% \pm 0.5\%$. This value is large but comparable to the scattering fraction of $>20\%$ found in IRAS 13349+2438 by Lee et al. (2013). A large scattering fraction suggests that SDSS J1352+4239 may be highly polarized. Considering the amount of polarization depends both on the geometry of the scattering source and the scattered fraction, SDSS J1352+4239 may exhibit polarization less than this value. Previous spectropolarimetry observations of BALQSOs revealed polarization reaching greater than $\sim 10\%$ in some objects (e.g., Brotherton et al. 1997; Ogle et al. 1999).

To test the necessity of the scattered flux component, we fit the data with a model that does not include it. The model fails to match the shape around ~ 2100–$2200\,\text{Å}$, creating a deeper Fe II trough.

Figure 8 shows the comparison between the best-fitting model and the model without the scattered component. Further discussion of possible origins of the scattered light is given in Section 7.1.

5.3. The Zero-velocity Component

We found a single prominent absorption feature between $2800\,\text{Å}$ and $2850\,\text{Å}$ that was not modeled with the blueshifted components (Figures 5 and 7). We identified this feature as Mg II $\lambda\lambda 2796, 2803$ lines with near zero-velocity offset and modeled it with a separate group of tophats bins. Seven tophat bins for the zero-velocity component span a velocity range from ~ -8900 km s^{-1} to ~ 6700 km s^{-1} with the total velocity width of $\sim 15,000$ km s^{-1}. The zero-velocity component seems to be most prominent in the Mg II lines, and this doublet is the only feature that is not blended significantly with the high-velocity lines. Our model also found the low-ionization lines Al III $\lambda\lambda 1854, 1862$ and Al II $\lambda 1670$ from the zero-velocity component to be present as shallow features in the spectrum at $\sim 1880\,\text{Å}$ and $\sim 1670\,\text{Å}$ with the Al II line being the shallower of the two.

Notably, we find no strong evidence for high-ionization absorption lines such as Si IV $\lambda\lambda 1402, 1393$, and C IV $\lambda\lambda 1548, 1550$ from the zero-velocity component in the data. That is, the high-velocity component alone produces enough opacity to match the data in the regions where the high-ionization lines from the zero-velocity component are expected to appear. This is very unusual since Al III and Mg II are always accompanied by high-ionization lines (e.g., Voit et al. 1993). Moreover, the high-ionization conditions that produce larger Al III opacity than Al II opacity for the zero-velocity component also predicts significant high-ionization lines.

We suspect that the gas cloud for the zero-velocity component is illuminated by a continuum that lacks the high-energy photons necessary to create such ions, because it has
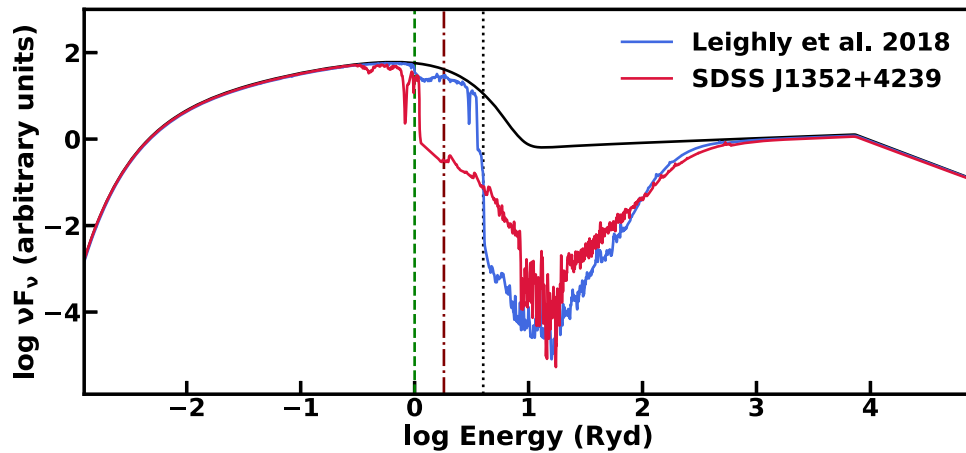
Figure 9. The unabsorbed AGN SED is plotted in black and the filtered SED generated from *Cloudy* with the physical parameters retrieved from the *SimBAL* fit of the blueshifted component is plotted in red. The filtered SED from SDSS J0850+4451 (Leighly et al. 2018) is plotted in blue as a comparison. The green dashed vertical line, brown dotted–dashed vertical line, and the black vertical dotted line show the ionizing potentials for H I, He I, and He II, respectively. SDSS J1352+4239 shows stronger attenuation in the Lyman continuum, as expected for high column density FeLoBAL, than the LoBAL SDSS J0850+4451, which has a thinner outflow that does not encompass the hydrogen ionization front.

been transmitted through the high-velocity part of the outflow. That is, in the presence of multiple gas clouds along a line of sight, the gas cloud farther from the radiation source may see an absorbed "filtered" SED from the back of the gas cloud that is located closer to the radiation source. This phenomenon has been investigated previously by Leighly et al. (2018). They explored the potential possibilities for the radiation filtering with SDSS J0850+4451 by creating synthetic spectra using the filtered SEDs. Both the accelerating and decelerating outflow scenarios with radiation filtering produced features that are not seen in the spectra of SDSS J0850+4451, and they concluded no support for the radiation shielding of outflowing gas in that object. Miller et al. (2018) analyzed the BAL troughs in LBQS 1206+1052 considering the possible "shading effect" using photoionization modeling and suggested that the two-phase model was consistent with the data but was not statistically distinguishable from a one-phase model. That is, the two-phase model was not required for the data. SDSS J1352+4239, on the other hand, seems to require an absorption component (zero-velocity component) originating from an absorbed SED to avoid creating the high-excitation ions at zero-velocity, and it is not possible to do so with an unabsorbed SED. The evidence is that we see several moderate to strong low-ionization absorption lines (e.g., Mg II, Al III) from the zero-velocity component, but the high-ionization lines normally associated with those lines are completely absent from the spectrum.

To test the filtering model, we first tried using a modified line list to model the zero-velocity component. We removed the high-ionization ion transitions (ionization potential >24.6 eV) to approximate such a condition. The results are not shown, but the success from this approach led to modeling with filtered continuum constructed following Leighly et al. (2018) Appendix A.2. We started with an unabsorbed SED redshifted to match the outflow velocity of the starting bin (highest-velocity bin and lowest-velocity bin for the decelerating outflow and accelerating outflow, respectively). Then, we created the first transmitted continuum from the starting bin with *Cloudy* and used the resulting transmitted continuum to illuminate the next adjacent bin for a subsequent *Cloudy* simulation to create the next transmitted continuum. The final filtered SED for the high-

velocity trough was calculated from the transmitted continuum of the final bin. A more detailed description of the construction of the filtered SED can be found in Leighly et al. (2018) Appendix A.2. We use the filtered SED from the accelerating outflow calculation because we do not find a significant difference between the accelerating and the decelerating outflow scenarios. Figure 9 shows how the filtered SED differs from the unfiltered AGN SED and how the filtered SED for SDSS J1352+4239, an FeLoBAL, differs from that of SDSS J0850+4451, a LoBAL. A new ionic column density grid was calculated using the filtered SED for the zero-velocity component.

We fixed the emission and high-velocity trough components from the preliminary best-fitting model and fit only the zero-velocity component with the new column density grid from the filtered continuum. The physical parameters for the new grid were allowed to vary as fitting parameters. Figure 10 shows how the zero-velocity component from the filtered SED produces sufficient low-ionization lines to match the data without overproducing high-ionization lines. The ionization parameters for the bins ranged between −2.8 and 1.8 with the filtered SED (Table 2). The uncertainties associated with the fit parameters and the range of values from the bins for the zero-velocity component were large mainly because the absorption feature is shallow and only a small number of lines are present in the spectrum.

In summary, the absorption feature centered around zero-velocity only showed absorption lines from low-ionization species. The zero-velocity component from an SED filtered by the high-velocity outflow provided a good fit by producing sufficient opacity for the low-ionization transitions without producing deep high-ionization absorption lines. The distinction between this result and previous ones looking for evidence for filtering or shading (Miller et al. 2018) is that while the previous efforts found that the data were consistent with filtering, our data show the lack of high-ionization lines that must be the signature of this phenomenon, and therefore require a filtered continuum.

6. Derived Physical Properties of the Outflow

Using *SimBAL*, we can measure the physical parameters of the outflow and the uncertainties associated with those values.
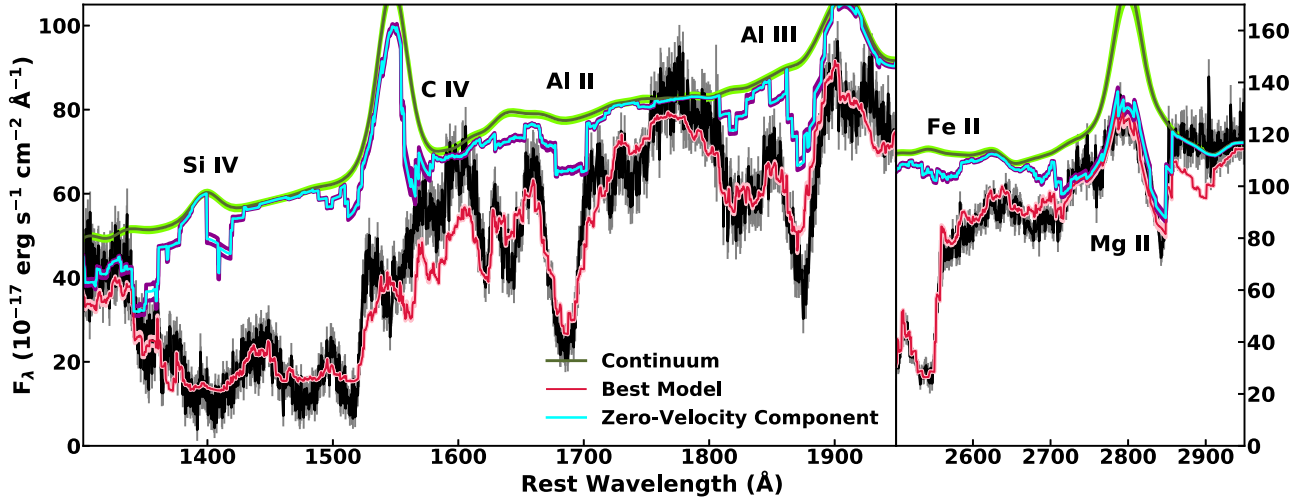
Figure 10. The cyan line represents the zero-velocity component model from the filtered grid. The filtered SED model produces sufficient opacity from the low-ionization ions (Mg II, Al III, and Al II) while high-ionization lines (C IV and Si IV) are suppressed.
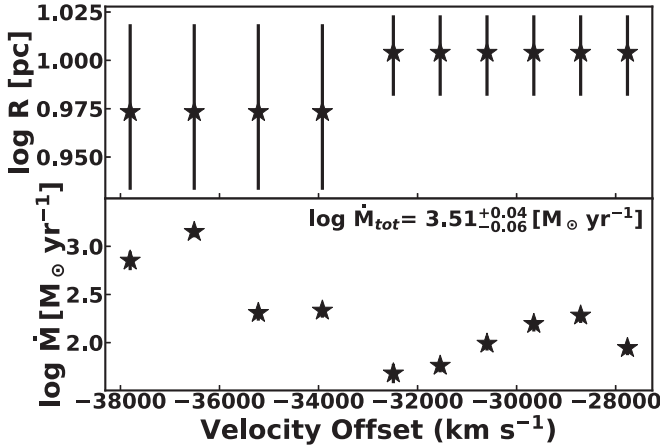

Figure 11. The radius and outflow mass estimates for each velocity bin. The outflowing wind is located ∼10 pc away from the central engine. The $\log n$ and $\log U$ values for the bins in the higher- and lower-velocity groups were constrained to have the same value. The total outflowing mass of 3200 ($M_\odot$ yr^{-1}) is noted on the bottom panel.

We extracted the radius of the outflow using the following relationship:

$$U = \frac{\phi}{nc} = \frac{Q}{4\pi R^2 nc},$$

where ϕ is the photoionizing flux in, photons s^{-1} cm^{-2}, and Q is the number of photoionizing photons per second emitted from the central engine. Therefore, with the density and ionization measurements from *SimBAL*, we can calculate the location of the outflow R. The value of Q was estimated by scaling the *Cloudy* input SED to the quasar spectrum and integrating the scaled SED for energies greater than the hydrogen ionization potential of 13.6 eV. We estimate log $Q = 57.3$–57.4 (photons s^{-1}) when scaled the flux density at 4000 Å ($F_{4000} = 72.58 \times 10^{-17}$ erg s^{-1} cm^{-2}Å^{-1}) and to the near-infrared (rest-optical) photometry points, respectively.

We derived the radius of each bin using the sets of physical parameters constrained by the tophat accordion model (Figure 11). We found that the location of the outflow is ∼10 pc away from the center.

Once we know the radius of the outflow, we can further calculate the mass outflow rate of the outflow and the kinetic luminosity associated with it. We computed the outflow mass using the equation from Dunn et al. (2010)

$$\dot{M} = 8\pi\mu m_p \Omega R N_{\mathrm{H}} v,$$

where the mean molecular weight is assumed to be $\mu = 1.4$, the global covering fraction is given by Ω, and R, N_{H}, and v are calculated from the best-fitting parameters from *SimBAL*. We calculate the mass outflow rate for each bin (Figure 11) and sum them to estimate the total mass outflow rate of log $\dot{M} = 3.5 \pm 0.04$ ($M_\odot$ yr^{-1}). The outflowing mass rate of 3210^{+270}_{-290} ($M_\odot$ yr^{-1}) is about 18 times the mass accretion rate (Section 3.5). We use $\Omega = 0.2$ based on the fraction of BALQs in optically selected surveys (e.g., Hewett & Foltz 2003), and further discussion of Ω is below.

Kinetic luminosity is one of the critical physical measures of the outflow strength. Cosmological simulations require the ratio between the kinetic luminosity and the bolometric luminosity to be 0.5%–5% for effective quasar feedback that could reproduce the observed scaling relations between the host galaxy and the central black hole (e.g., Di Matteo et al. 2005; Hopkins & Elvis 2010). Using the equation $\dot{E}_k = \dot{M}v^2/2$, we measure the log kinetic luminosity to be 48.1 ± 0.04 (erg s^{-1}) and $L_{\mathrm{KE}}/L_{\mathrm{Bol}}$ of ∼1. This value of kinetic luminosity is the largest ever found from BAL quasars and sets a new record for the strength of the quasar outflowing wind. We compare with other large L_{KE} outflows in Section 7.3.

In the above mass outflow and kinetic luminosity calculations, we adopted the commonly used value of 0.2 for global covering fraction (Ω) following Hewett & Foltz (2003) who found 20% of the optically selected quasars to have broad absorption lines (once selection effects were accounted for). The typical values for global covering factor, or the BAL fraction, range from 0.2 to 0.4 depending mainly on the sample selection criteria (e.g., Weymann et al. 1991; Trump et al. 2006; Dai et al. 2008; Knigge et al. 2008; Allen et al. 2011). One explanation for BALs is that they are present in all quasars, covering 20% ∼ 40% of the solid angle, and that the fraction of objects with BAL features reflect the amount of sky covered by the quasar outflows in an individual object.
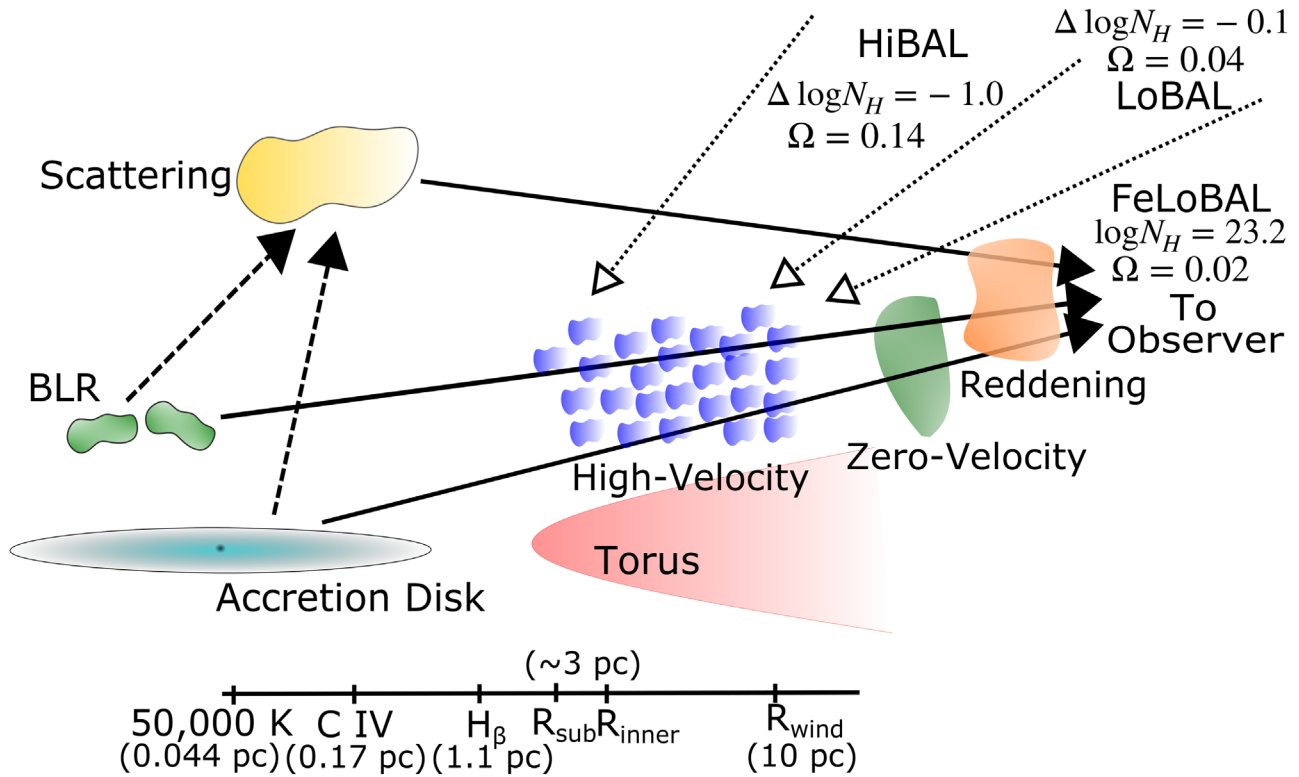
Figure 12. This cartoon illustrates how each spectral model component corresponds to different physical AGN components around the central black hole. The dashed lines represent the photons reaching the scattering medium to create the scattered flux, and the solid lines represent the photons reaching the observer. The dotted lines represent different sightlines for HiBAL, LoBAL, and FeLoBAL quasars (Section 6). The changes in column density ($\log N_H$) required to transform the spectrum from FeLoBAL to the other types and the different global covering fractions (Ω) are labeled on the figure. The main BAL cloud is located slightly farther away from the central engine than the innermost edge of the torus, and the zero-velocity cloud must be located between the main cloud and the reddening source. The horizontal bar at the bottom of the figure represents the location on the accretion disk where the temperature is about 50,000 K (Section 7.2), the locations of the C IV and Hβ emitting broad-line regions (Section 3.5), the distances to the torus, and the outflowing wind (R_{inner}, R_{sub}, and R_{wind}; Section 7.1).

Supporting this view is the fact that (Hi)BALQs have a similar broadband spectral energy distribution as normal quasars (e.g., Gallagher et al. 2002, 2006, 2007). However, the above number is derived from HiBALs with C IV lines, and LoBAL fractions can be as low as ~1% in a quasar sample (e.g., Trump et al. 2006; Dai et al. 2012). Assuming this is the case, we would infer the global covering fraction for (Fe)LoBALs to be as low as ~0.01.

FeLoBALs can be difficult to identify in the general quasar population due to their lack of strong emission lines, and their population fraction might not necessarily reflect the realistic sky coverage of the FeLoBAL wind. Dunn et al. (2010) discuss this particular issue in detail and concluded that a selection effect is the reason for the low LoBAL fraction. They used the value of (Hi)BAL fraction as the global covering fraction for FeLoBAL outflows. They assert that LoBALs and HiBALs are coming from physically similar outflowing gas, but we observe LoBAL features from the gas because the light of sight (LOS) happens to pass through the edge of dusty torus. This not only explains the additional reddening in LoBALs (e.g., Sprayberry & Foltz 1992; Reichard et al. 2003) but also the low LoBAL fraction because the LOS needs to be precisely at an angle where it passes through enough torus to produce low-ionization lines but not obscure the broad-line region.

Finding the true value for BAL fraction or the global covering fraction is difficult and often uncertain. For example, a large BAL quasar fraction of about ~40% has been found from a luminous infrared selected sample (Dai et al. 2008).

This value is about double of what Hewett & Foltz (2003) found from the optically selected sample, but this discrepancy is not very surprising considering BALQs tend to be more frequently reddened than non-BALQs (Krawczyk et al. 2015). Therefore, in principle, one can adopt the value of global covering fraction as large as 0.4 for all BALs or as low as 0.01 for FeLoBALs depending on the assumption made to translate the statistical BAL fractions into global covering fractions.

Instead of using a single global covering fraction, we constructed a model to explore the idea that a single outflow exists in the vicinity of the central engine and multiple sightlines observe the outflowing gas as different types of BALs (e.g., HiBAL, LoBAL, or FeLoBAL) depending on the viewing angle and the column density the sightline passes through (Figure 12). We estimated the mass outflow rate according to this scenario by gradually lowering the column densities of all the bins by the same small amount while keeping all other parameters fixed to mimic the effect of sightlines passing through less outflowing gas material. Specifically, we lowered the $\log N_H$–$\log U$ column density parameter and recorded the parameters when the model no longer produced Fe II absorption lines and transformed to a LoBAL. We continued lowering the $\log N_H$–$\log U$ column density parameter until the Mg II absorption lines disappeared to create an HiBAL. From this exercise, we were able to estimate $\log N_H$ values for different sightlines that can produce different BAL spectral types of the same outflowing cloud responsible for the trough in SDSS J1352+4239 ($N_{H\,HiBAL}$ and

$N_{H\,LoBAL}$). We then modify the use of single global covering fraction with the following equation:

$$\Omega N_H \Rightarrow \Omega_{HiBAL} N_{H\,HiBAL} + \Omega_{LoBAL} N_{H\,LoBAL}$$
$$+ \Omega_{FeLoBAL} N_{H\,FeLoBAL}.$$

Using the result from Dai et al. (2012), we set Ω_{HiBAL}, Ω_{LoBAL}, and $\Omega_{FeLoBAL}$ to be 0.14, 0.04, and 0.02, respectively.

Figure 12 shows the result of our exercise with the changes in the column density noted in the illustration. We obtain log L_{KE} of $\sim$47.6 (erg s^{-1}) following the above interpretation. We conclude that the true value lies between 47.6 (computed using the scenario described here and in Figure 12) and 48.4 (computed using the maximum value $\Omega = 0.4$ from Dai et al. 2008). Applying the same method, we obtain the range of mass outflow rate log $\dot{M} = 3.0$–3.8 ($M_\odot$ yr^{-1}). We note that the current version of *SimBAL* that uses the grids calculated from the version C17 of *Cloudy* is only available for the solar metallicity. A higher-metallicity grid would yield a smaller column density and, therefore, a smaller outflow rate (Leighly et al. 2018).

7. Discussion

7.1. A Plausible Geometry of the Outflows

In Section 6, we found the radius of the outflow to be approximately 10 pc. Using the equation $R_{\tau k} = 0.47(6\nu L_\nu(V))/(10^{46}\,\mathrm{erg\,s^{-1}})$ from Kishimoto et al. (2007), derived from near-infrared reverberation monitoring, we estimated the distance to the innermost edge of the torus to be 3.5 pc. Furthermore, we estimated the dust sublimation radius $R_{sub} \simeq 2.0$ pc using the equation $R_{sub} = 0.2 L_{46}^{1/2}$ pc from Laor & Draine (1993). This indicates that the outflow is located in the vicinity of the dusty torus.

Section 5.3 describes the radiation shielding in the zero-velocity component and how this gas must be farther from the central engine than the main high-velocity outflow gas. Considering both the kinematics and the peculiar ionization condition of the absorber, it is possible that the the zero-velocity absorption feature might be arising from an infalling gas cloud. Hall et al. (2013) analyzed a sample of objects that show redshifted C IV absorption features and suggested that such absorption signatures can originate from infalling clouds or rotating disk winds. SDSS J1352+4239, on the other hand, does not show any redshifted high-ionization lines like the sample Hall et al. (2013) studied, so it is not possible to use their interpretation of the phenomenon directly. Also, none of the objects in their sample shows strong blueshifted troughs; therefore, it is possible that the physical conditions in SDSS J1352+4239 are very different from their objects. We speculate that this potential infalling gas could be originating from an earlier ejection episode, and we are seeing the signature of the infalling remnant.

Figure 12 shows a physical picture of our spectral model. From analyzing the best-fitting spectral model, we know the location of the BAL outflow is near the torus. Both the absorbed spectrum and the scattered flux are reddened, so the dusty reddening source must lie at a larger radius. The zero-velocity component must be located between the main outflow and the reddening source as the reddening source would transmit too few ionizing photons. We constrained the ionization parameters for the zero-velocity component to be log $U < 1.8$, and this implies that we can estimate the density

of log $n < 5.0$ (cm^{-3}) in order for the gas to be located farther than the high-velocity outflow gas. We do not have enough information from the spectrum to determine the exact geometry of the scattering cloud. Potential follow-up spectropolarimetry observations may help us gain an insight into the geometry of some of the physical components in SDSS J1352+4239 we discussed throughout the paper.

7.2. Acceleration Mechanisms

We calculated the momentum flux of the outflow from the equation $\dot{P} = \dot{M}v$ (e.g., Faucher-Giguère et al. 2012), and we found log $\dot{P}$ of 38.85±0.04 (dyne) (38.36–39.15 following the global covering fraction interpretation in Section 6 and Figure 12) with each individual bin having log $\dot{P}$ of 37–38.5. Compared to log L_{Bol}/c of 37.5, we find that the ratio between the momentum flux of the outflow and the photon flux is around 20. The ratio of 20 is far greater than what is expected of the momentum-conserving wind, where the maximum momentum flux of the outflow for a single scattering is L_{Bol}/c, or a momentum flux ratio of $\sim$1 (e.g., Fiore et al. 2017). Two mechanisms have been proposed for objects with large log $\dot{P}$. In the energy-conserving scenario, the outflowing winds get an additional push by the shocks generated from ISM interactions (e.g., Faucher-Giguère & Quataert 2012). Such a mechanism can generate a momentum boost and increase the momentum flux ratio between the outflowing gas and radiation by an order of magnitude. King & Pounds (2015) discuss various acceleration mechanisms for AGN outflows and compare the size scales of the energy-conserving outflows and the momentum-conserving outflows. An energy-conserving mechanism mainly explains the $\sim$kpc size scale outflows where the Compton cooling timescale becomes greater than the flow timescale, and the full energy of the fast nuclear wind is communicated due to inefficient cooling (e.g., King et al. 2011). The Compton cooling time for SDSS J1352+4239 is $t_c \simeq 1.16 \times 10^5 R_{kpc}^2 \simeq 12$ yr (King et al. 2011, Equation (7)), and we can calculate the flow time $t_{flow} = \frac{R}{v} \simeq 330$ yr ($R \sim 10$ pc, $v \sim 0.1c$). It is unlikely for the outflow in SDSS J1352+4239 to be accelerated via energy-conserving mechanism, because the cooling is still effective, up to $R \sim 50$ pc, and the outflow we found is a compact torus scale outflow ($R \sim 10$ pc). The other mechanism involves scattering by dust, which has a larger scattering cross section than resonance scattering by ions (e.g., Fabian et al. 2008, 2018). Based on the size scale and the reddening observed in SDSS J1352+4239, it seems plausible that the outflow is a momentum-conserving wind with the additional momentum being harnessed by the dust. Thompson et al. (2015) points out that if the effective infrared optical depth is significantly large at the cloud launch point, the outflowing gas can have a momentum ratio greater 1 with the momentum-conserving mechanism.

We further explored the acceleration mechanism responsible for the high-velocity outflow using force multiplier (FM) analysis. The FM is defined as the ratio of the total cross-section to the Thompson cross-section.

We used the best-fit parameters from the model and *Cloudy* to calculate the FM values for each bin. Figure 13 shows the FM values as a function of velocity. In order for radiative driving of absorbers to occur, FM $\geqslant (L_{Edd}/L_{Bol})^{-1}$ is a necessary condition (e.g., Netzer 2013). Leighly et al. (2018) calculated the FM values for their *SimBAL* model of LoBAL object SDSS J0850 +4451 and found that not all tophat bins satisfied the above condition and suggested that alternative driving mechanism
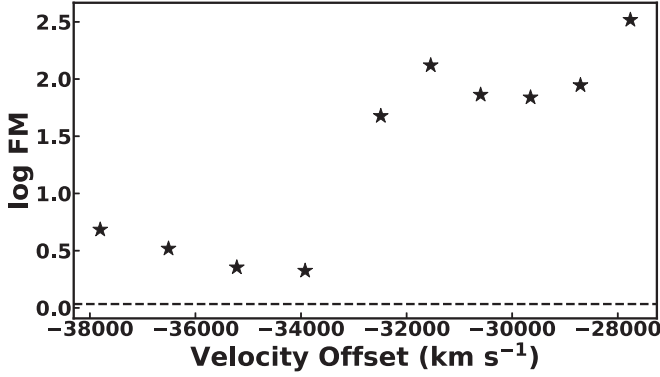
Figure 13. The force multiplier (FM) values computed for each bin using *Cloudy*. The horizontal dashed line represents FM = L_{Edd}/L_{Bol} above which the absorber can be radiatively driven. Because SDSS J1352+4239 is radiating at near Eddington limit, the FM threshold necessary for the radiative driving is low (~1) and the FM values for each bin are also rather higher due to lower-ionization parameters. For comparison, see Figure 17 in Leighly et al. (2018) for LoBAL object SDSS J0850+4451.

Figure 14. The wind terminal velocities for different inner wind radii (r_l = 5.0 and 0.1 pc in black stars and orange circles, respectively) have been calculated for each bin from the force multiplier (FM) values. The horizontal gray shaded region shows the actual outflow velocity range observed in SDSS J1352 +4239. The lower-velocity bins can get enough acceleration from large FM values and reach the high outflow velocity that we see in the spectra even when launched at a large inner wind radius (5 pc) near the current location of the outflow; however, the higher-velocity bins have small FM values (Figure 13) and can only reach high velocity with a smaller launch radius (0.1 pc).

might be necessary. However, SDSS J0850+4451 is radiating at only 6% L_{Edd}. SDSS J1352+4239, on the other hand, is radiating near the Eddington limit (log (L_{Edd}/L_{Bol}) ~ 0); therefore, even with lower FM values, the absorber can be radiatively driven, as all 10 bins have FM values greater than (L_{Edd}/L_{Bol})$^{-1}$. This intuitively makes sense since the radiative driving relies on the power of radiation relative to the black hole mass. The FM values are smaller for the higher-velocity bins because they have higher ionization parameters. Photoionized gas with higher ionization will have fewer ions that can provide UV line opacity and therefore have lower FM.

FM values alone do not fully explain how the main outflow in SDSS J1352+4239 was able to reach its high-velocity and large momentum ratio with a large outflow mass. Therefore, we used the equation of motion to further probe how much radiative acceleration can be obtained with the given FM values we found for the main outflow in SDSS J1352+4239. We use the equation for acceleration,

$$v\frac{dv}{dR} \simeq \frac{M(R)\sigma_T L}{4\pi R^2 m_p c} - \frac{GM_{BH}}{R^2}$$

where the first term represents the radiative acceleration with the FM ($M(R)$) and the second term is the force of gravity from the black hole. Integrating this equation assuming a constant FM value (FM), we retrieve the following equation:

$$v_\infty = 32,000 R_{0.1}^{-1/2}(6.69 \times 10^{-3} L_{46} FM - 0.008 M_8)^{1/2} \text{ km s}^{-1}$$

where v_∞ is the wind terminal velocity, $R_{0.1}$ is the inner wind radius or the launch radius in units of 0.1 pc, L_{46} is the luminosity of the quasar in the units of 10^{46} erg s^{-1}, and M_8 is the black hole mass in units of $10^8 M_\odot$. Figure 14 shows the wind velocities calculated from the above equation.

The wind velocities for the lower-velocity bins can reach the observed outflow velocities with the launch radius ($r_l \sim 5.0$ pc), similar to where we find the outflow ($r \sim 10$ pc). But the higher-velocity bins require a much smaller launch radius ($r_l < 0.1$ pc) to match the outflow velocity seen in the spectra. At such a small radius, we expect the gas to be more highly ionized and have a smaller FM value. Therefore, if we compute the integral with FM as a function of radius, then the lower-velocity bins would need an even smaller inner wind radius to be
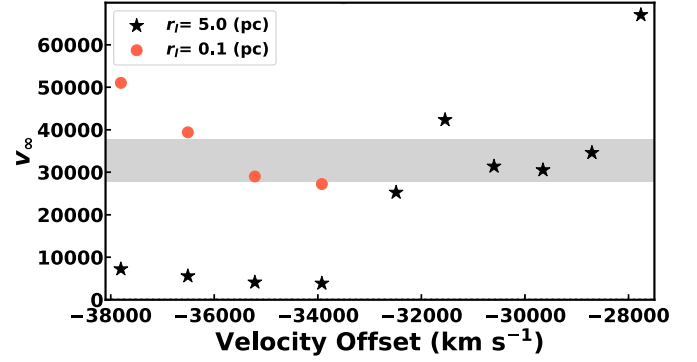
able to reach a high outflow velocity. Note that the above FM values do not include the opacity from the dust. However, with the presence of dust, the total opacity will increase significantly and as a consequence, the gas will be able to obtain extra acceleration. It will enable the lower-velocity bins to potentially reach high velocities even at a larger radius.

Another useful size scale is the location of the UV emission of the accretion disk. The radiation-driven disk winds are thought to be accelerated by the absorption of energetic photons from the UV radiation of the accretion disk (e.g., Proga & Kallman 2004). The radius at which the disk radiation is mostly in the UV and the location on the accretion disk where the temperature is about 50,000 K is considered the outflow launch radius for such winds (e.g., Giustini & Proga 2019). We calculated the location of 50,000 K emission of the accretion disk for SDSS J1352+4239 to be 0.044 parsec, using the equation $T(R) = (3GM\dot{M}/8\pi R^3\sigma)^{1/4}$ where σ is the Stefan–Boltzmann constant, M is the mass of the black hole, and $\dot{M}$ is the accretion rate. This value is significantly smaller than the location of the outflow. Assuming constant outflow velocity of −30,000 km s^{-1}, it would take about 320 yr for the outflow to reach its current location of 10 pc if the gas was launched at 50,000 K emission region of the accretion disk. The value is substantially larger than the rough estimate of the cloud dissipation time (e.g., Hamann et al. 2013, $t \sim \Delta R_{Cloud}/\Delta v \sim$ 10s yr for SDSS J1352+4239). Therefore, we suspect the outflow is being radiatively driven by both the absorption lines and dust, launched near the torus at a large distance away from the disk.

For example, Czerny et al. (2017) discuss a failed radiatively accelerated dusty outflow (FRADO) model to understand the motion of the clouds within the broad-line region. Their model is for the broad-line region, but it is possible that some of the clouds elevated by radiation pressure from the disk or dust would be entrained into the outflow. And these dusty gas clouds with high opacity can form an outflow that can potentially create BAL troughs.

7.3. Comparison with Other Known Energetic Quasar Outflows

We compared our results with other exceptionally energetic outflows in the literature (Table 3). Borguet et al. (2013) found

Table 3
Comparison with Other BAL Quasar Outflows

Object	$\log L_{\mathrm{Bol}}$ (erg s^{-1})	$\log M_{\mathrm{BH}}$ ($M_\odot$)	$\dot{M}$ ($M_\odot$ yr^{-1})	$\log L_{\mathrm{KE}}$ (erg s^{-1})	Ω	Reference
SDSS J1106+1939 (LoBAL)	47.2	8.9	390^{+300}_{-10}	$46.0^{+0.3}_{-0.1}$	0.08	Borguet et al. (2013)
SDSS J0831+0354 (LoBAL)	46.9	8.8	410^{+530}_{-220}	$45.7^{+0.3}_{-0.4}$	0.08	Chamberlain et al. (2015)
HE 0238-1904 (HiBAL)	47.2	⋯	69^{+50}_{-50}	$45.4^{+0.3}_{-0.6}$	0.5	Arav et al. (2013)
APM 08279+5255 (UFO)	47.45	10.0	11.2	46.9	⋯	Chartas et al. (2009), Fiore et al. (2017)
SDSS J1352+4239 (FeLoBAL)	48.0	9.9	1040–6460	47.6–48.4	see Section 6	This work

Note. The mass outflow rate and the kinetic luminosity of the outflow in SDSS J1352+4239 were estimated using multiple global fractions (Section 6).

an outflow with $\log L_{\mathrm{KE}}$ of at least 46 (erg s^{-1}) in SDSS J1106+1939, and it was the most energetic BALQSO outflow ever reported at the time of publication. SDSS J0831+0354 was also discovered to have a strong outflow with $\log L_{\mathrm{KE}} = 45.7$ (erg s^{-1}; Chamberlain et al. 2015). Since their discovery, several more BAL quasars with comparable energetics have been found. Fiore et al. (2017) collected a large sample of AGN outflow data and performed a quantitative analysis on the properties of the outflows. Some ultra-fast outflow (UFO) objects with absorption lines in the X-ray band have strong winds in their systems due to the high velocity of the outflows. APM 08279+5255 is a lensed quasar with an X-ray UFO feature that has a near-relativistic outflow with $\log L_{\mathrm{KE}} = 46.85$ (erg s^{-1}; Chartas et al. 2009). The energy of the outflows we discovered in SDSS J1352+4239 is greater than even the most energetic UFO outflow known. Estimating the outflow radius is crucial in estimating the kinetic luminosity of the outflows, and it is worth noting that the outflow radius calculation for UFOs are different from the BALQs. To estimate the radius, the density of the gas needs to be carefully constrained. For BAL spectra, the density of the gas can be directly constrained by analyzing the density-sensitive absorption lines. On the other hand, UFOs and X-ray spectra rely on an indirect method where the density is estimated by interpreting the trough variability (e.g., Risaliti et al. 2002; Hemler et al. 2019). Among the objects listed in Table 3, SDSS J1352+4239 is the only FeLoBAL object and the most luminous. FeLoBAL objects are known to have higher column density relative to the hydrogen ionization front (Lucy et al. 2014) than the other BAL objects, and it is possible that in a large FeLoBAL sample, we might be able to find more BAL objects with comparable or more energetic outflows (H. Choi et al. 2020, in preparation; C. Dabbieri et al. 2020, in preparation).

7.4. How Special Is SDSS J1352+4239?

SDSS J1352+4239 is a very luminous quasar with an energetic outflow and an impressive overlapping trough feature in the rest-UV spectrum. The quasar luminosity function shows that such luminous quasars are rare objects in the universe with space densities $1 \sim 2$ orders of magnitude lower than the less-luminous quasars (Richards et al. 2006b). Moreover, fewer than half of quasars show BAL features (e.g., Hewett & Foltz 2003 ($\sim$20%); Dai et al. 2008 ($\sim$40%)) and among the BAL quasars, only a handful of objects show features of very powerful outflows (e.g., Fiore et al. 2017). This means one can find only about $2 \sim 4$ luminous BALQs that may potentially have strong outflows from a sample of 1000 quasars and a sample of at least tens of thousands quasars is needed to find

one luminous quasar with such a high-velocity FeLoBAL outflow. From these statistics, we can infer that SDSS J1352+4239 is indeed a rare and special kind of object.

Observational survey programs and the pipelines they use have biases and observational limitations that would result in under-reporting of the BAL quasars with strong outflows or peculiar spectroscopic features (extreme BAL troughs, heavy reddening, and low luminosity and signal-to-noise ratio). BALQSOs with strong absorption from thick absorbing gas often do not show any strong emission features, making it difficult for survey pipelines to correctly categorize them as quasars. Strong reddening not only dims the object but it can further make the spectra more difficult to analyze and classify. More BAL objects similar to SDSS J1352+4239 may already be in the publicly available archives.

7.5. Implications for AGN Feedback and Evolution

Theoretical model calculations require outflows to have the kinetic luminosities of about $0.5\% \sim 5\%$ of the bolometric luminosity to contribute to AGN feedback and influence the star formation in the host galaxies (e.g., Scannapieco & Oh 2004; Di Matteo et al. 2005; Hopkins & Elvis 2010). The energy in the outflow we discovered in SDSS J1352+4239 is roughly the same as the quasar bolometric luminosity, and we can confidently conclude that the outflow has more than enough energy to influence the star formation in the host galaxy and provide feedback. The strength of the outflow (L_{KE}) is thought to scale with the bolometric luminosity of the quasar (e.g., Zubovas & King 2012; Costa et al. 2014). SDSS J1352+4239 has a very high bolometric luminosity, greater than most of the quasars known to have extreme AGN luminosities (e.g., Bischetti et al. 2017, WISE/SDSS selected hyper-luminous (WISSH) quasars), and the observed energetic outflow (Sections 6, 3.5), which seems to support this conjecture.

Some extremely red quasars are also found to have high bolometric luminosities and a fraction of them are known to host strong outflows (e.g., Hamann et al. 2017; Zakamska et al. 2019). Urrutia et al. (2009) found an anomalously large fraction of BALs (LoBALs) in a sample of red quasars, and they argue that the LoBAL quasars represent quasars in their early evolutionary stage. They further suggest the idea that the BAL outflows occur just after the merger events during a "blow out" phase, which suppresses the star formation in the host galaxy. Obscured quasars are expected to show signs of ongoing merger activities and/or signatures of a recent starburst episode (Sanders et al. 1988); however, the observational evidence shows mixed evidence for merger activities or starbursts (e.g., Violino et al. 2016; Zakamska et al. 2019).
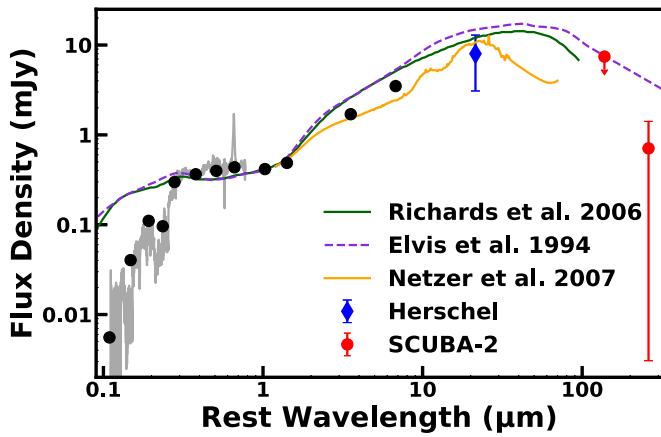
Figure 15. The broadband photometry data for SDSS J1352+4239 is plotted with mean quasar SEDs from Richards et al. (2006a) and Elvis et al. (1994). Both of these SEDs do not account for star formation, so the quasar intrinsic SED from Netzer et al. (2007) is plotted in orange as well. Black dots are the photometry data from SDSS, 2MASS, and *WISE* as described in Section 4 and shown in Figure 3. The blue dot is the photometry data from *Herschel* at 70 μm, observed frame. The red dots are the SCUBA-2 data from Violino et al. (2016) at 850 and 450 μm, observed frame. The *WISE* photometry points and *Herschel* observation of SDSS J1352+4239 are consistent with the intrinsic quasar SED. The starburst component would dominate the SED at around 100 μm if there were enhanced star formation in this quasar (e.g., Farrah et al. 2012). We do not see such a far-infrared excess and therefore conclude that there is no strong starburst contribution in SDSS J1352+4239.

SDSS J1352+4239 does not show a signature of substantial star formation. Violino et al. (2016) used the Submillimetre Common-User Bolometer Array 2 (SCUBA-2) to investigate whether FeLoBALs represent an evolutionary step between ultraluminous infrared galaxies (ULIRGs) and unobscured quasars. They found no evidence for enhanced star formation in FeLoBALs including SDSS J1352+4239. SDSS J1352+4239 was also observed by ESA *Herschel Space Observatory* (Pilbratt et al. 2010)[13] with PACS (Poglitsch et al. 2010) and SPIRE (Griffin et al. 2010), and was detected with PACS at 70 μm. We obtained the PACS data from the *Herschel* Science Archive.[14] The infrared data are plotted in Figure 15 along with composite quasar SEDs from Richards et al. (2006a), Elvis et al. (1994) and Netzer et al. (2007). No far-infrared excess is detected. Therefore, the photometry data do not support the need for an extra SED component from a starburst.

8. Summary

In recent years, several discoveries of powerful AGN outflows have been made (e.g., Chartas et al. 2009; Borguet et al. 2013; Fiore et al. 2017). A number of such discoveries were made from the studies of X-ray observations or emission lines in the optical or mm bands. UV outflows from BAL quasars have received less attention even though their discovery predates the other channels by decades. There has not been a well-defined statistical analysis of the BAL absorbers primarily due the complex nature of the BAL spectra. *SimBAL* (Leighly et al. 2018) enables the first quantitative and systemic studies of UV BAL outflows and their potential for feedback. With *SimBAL*, we were able to analyze the complex absorption features in the overlapping

trough quasar spectrum of SDSS J1352+4239 and discover the most energetic AGN wind discovered to date with log kinetic luminosity of 48.1 ± 0.04 (erg s^{-1}). Our principal results are as follows:

1. In Section 3.4, we used Hα to measure the true redshift of 2.2639 ± 0.0008, a value about $\Delta z \sim 0.25$ larger than the previously reported values for SDSS J1352+4239. The true redshift led to the discovery of the extreme velocity of the outflow.

2. The black hole mass calculated from the Hβ line is $8.6 \times 10^9 \, M_\odot$ and L_{Edd} for the given black hole mass is 1.08×10^{48} (erg s^{-1}) (Section 3.5). SDSS J1352+4239 is radiating near the Eddington limit with log $L_{\mathrm{Bol}} = 48.0$ (erg s^{-1}) with the mass accretion rate of 176 $M_\odot$ per year (Section 4.1).

3. In Section 5, we discussed the kinematics and the physical conditions associated with the outflow in SDSS J1352 +4239. Our model finds the maximum wind velocity of $\sim -38{,}000$ km s^{-1}, making it the fastest FeLoBAL outflow ever found. We estimate the total covering fraction-weighted column density of log $N_{\mathrm{H}} = 23.22 \pm 0.05$ (cm^{-2}).

4. In Section 6, we measured the mass outflow rate of 3210^{+270}_{-290} ($M_\odot$ yr^{-1}) with the global covering fraction $\Omega = 0.2$. The mass outflow rate is about 18 times higher than the mass accretion rate. We found that this outflow has the largest kinetic luminosity ever found with log $L_{\mathrm{KE}} = 48.1 \pm 0.04$ (erg s^{-1}). For an estimated log L_{Bol} of 48 (erg s^{-1}), we calculate the ratio $L_{\mathrm{KE}}/L_{\mathrm{Bol}} \sim 1$, much greater than the 0.5%–5% thought to be sufficient to contribute to galaxy feedback.

5. We report the first definitive case where the data require a model component generated from a filtered SED, providing a strong support for the radiation shielding in action (Section 5.3). We conclude that this additional absorber is being irradiated with the AGN SED but with a significant amount of ionizing photons taken out by the fast outflow located closer to the central engine.

6. In Section 7.1, we found that the outflow is located near the torus. However, the ratio between the outflow momentum flux and the quasar photon flux is far greater than unity ($\sim$20), expected for nuclear/torus scale outflows, suggesting that the extra source of momentum boost is required to explain the dynamics of the outflow we see in SDSS J1352+4239. The dust in the environment near the torus could potentially serve as the acceleration mechanism (Section 7.2).

Currently, we are analyzing a sample of FeLoBAL objects with *SimBAL* (H. Choi et al. 2020, in preparation), and further effort toward creating a large sample of quasars with FeLoBAL outflows using machine-learning techniques is currently underway (C. Dabbieri et al. 2020, in preparation).

---

[13] PI: Meisenheimer, "The Dusty Young Universe: Photometry and Spectroscopy of Quasars at $z > 2$."
[14] http://archives.esac.esa.int/hsa/whsa

ORCID iDs

Hyunseop Choi ● https://orcid.org/0000-0002-3173-1098
Karen M. Leighly ● https://orcid.org/0000-0002-3809-0051
Donald M. Terndrup ● https://orcid.org/0000-0002-0431-1645
Gordon T. Richards ● https://orcid.org/0000-0002-1061-1804

References

Allen, J. T., Hewett, P. C., Maddox, N., Richards, G. T., & Belokurov, V. 2011, MNRAS, 410, 860
Arav, N., Borguet, B., Chamberlain, C., Edmonds, D., & Danforth, C. 2013, MNRAS, 436, 3286
Arav, N., Kaastra, J., Kriss, G. A., et al. 2005, ApJ, 620, 665
Barlow, T. A., & Sargent, W. L. W. 1997, AJ, 113, 136
Bautista, M. A., Dunn, J. P., Arav, N., et al. 2010, ApJ, 713, 25
Bentz, M. C., Denney, K. D., Grier, C. J., et al. 2013, ApJ, 767, 149
Bischetti, M., Piconcelli, E., Vietri, G., et al. 2017, A&A, 598, A122
Borguet, B. C. J., Arav, N., Edmonds, D., Chamberlain, C., & Benn, C. 2013, ApJ, 762, 49
Brotherton, M. S., Tran, H. D., van Breugel, W., Dey, A., & Antonucci, R. 1997, ApJL, 487, L113
Cardelli, J. A., Clayton, G. C., & Mathis, J. S. 1989, ApJ, 345, 245
Chamberlain, C., Arav, N., & Benn, C. 2015, MNRAS, 450, 1085
Chartas, G., Saez, C., Brandt, W. N., Giustini, M., & Garmire, G. P. 2009, ApJ, 706, 644
Cohen, M., Wheaton, W. A., & Megeath, S. T. 2003, AJ, 126, 1090
Cohen, M. H., Ogle, P. M., Tran, H. D., et al. 1995, ApJL, 448, L77
Collin, S., Kawaguchi, T., Peterson, B. M., & Vestergaard, M. 2006, A&A, 456, 75
Costa, T., Sijacki, D., & Haehnelt, M. G. 2014, MNRAS, 444, 2355
Cushing, M. C., Vacca, W. D., & Rayner, J. T. 2004, PASP, 116, 362
Czerny, B., Li, Y.-R., Hryniewicz, K., et al. 2017, ApJ, 846, 154
Dai, X., Shankar, F., & Sivakoff, G. R. 2008, ApJ, 672, 108
Dai, X., Shankar, F., & Sivakoff, G. R. 2012, ApJ, 757, 180
de Kool, M., Arav, N., Becker, R. H., et al. 2001, ApJ, 548, 609
de Kool, M., Becker, R. H., Arav, N., Gregg, M. D., & White, R. L. 2002a, ApJ, 570, 514
de Kool, M., Becker, R. H., Gregg, M. D., White, R. L., & Arav, N. 2002b, ApJ, 567, 58
Di Matteo, T., Springel, V., & Hernquist, L. 2005, Natur, 433, 604
DiPompeo, M. A., Brotherton, M. S., & De Breuck, C. 2011, ApJS, 193, 9
Dunn, J. P., Bautista, M., Arav, N., et al. 2010, ApJ, 709, 611
Elvis, M., Wilkes, B. J., McDowell, J. C., et al. 1994, ApJS, 95, 1
Fabian, A., Ricci, C., & Ishibashi, W. 2018, 42nd COSPAR Scientific Assembly, E1.13-29-18
Fabian, A. C., Vasudevan, R. V., & Gandhi, P. 2008, MNRAS, 385, L43
Farrah, D., Urrutia, T., Lacy, M., et al. 2012, ApJ, 745, 178
Faucher-Giguère, C.-A., & Quataert, E. 2012, MNRAS, 425, 605
Faucher-Giguère, C.-A., Quataert, E., & Murray, N. 2012, MNRAS, 420, 1347
Ferland, G. J., Chatzikos, M., Guzmán, F., et al. 2017, RMxAA, 53, 385
Fiore, F., Feruglio, C., Shankar, F., et al. 2017, A&A, 601, A143
Foltz, C. B., Chaffee, F. H., Hewett, P. C., Weymann, R. J., & Morris, S. L. 1990, BAAS, 22, 806
Foreman-Mackey, D., Hogg, D. W., Lang, D., & Goodman, J. 2013, PASP, 125, 306
Francis, P. J., Hewett, P. C., Foltz, C. B., et al. 1991, ApJ, 373, 465
Freeman, P., Doe, S., & Siemiginowska, A. 2001, Proc. SPIE, 4477, 76
Fynbo, J. P. U., Krogager, J. K., Venemans, B., et al. 2013, ApJS, 204, 6
Fynbo, J. P. U., Møller, P., Heintz, K. E., et al. 2020, A&A, 634, A111
Gallagher, S. C., Brandt, W. N., Chartas, G., et al. 2006, ApJ, 644, 709
Gallagher, S. C., Brandt, W. N., Chartas, G., & Garmire, G. P. 2002, ApJ, 567, 37
Gallagher, S. C., Richards, G. T., Lacy, M., et al. 2007, ApJ, 661, 30
Giustini, M., & Proga, D. 2019, A&A, 630, A94
Goobar, A. 2008, ApJL, 686, L103
Griffin, M. J., Abergel, A., Abreu, A., et al. 2010, A&A, 518, L3
Hall, P. B., Anderson, S. F., Strauss, M. A., et al. 2002, ApJS, 141, 267
Hall, P. B., Brandt, W. N., Petitjean, P., et al. 2013, MNRAS, 434, 222
Hamann, F., Chartas, G., McGraw, S., et al. 2013, MNRAS, 435, 133
Hamann, F., Chartas, G., Reeves, J., & Nardini, E. 2018, MNRAS, 476, 943
Hamann, F., Zakamska, N. L., Ross, N., et al. 2017, MNRAS, 464, 3431
Hazard, C., McMahon, R. G., Webb, J. K., & Morton, D. C. 1987, ApJ, 323, 263
Hemler, Z. S., Grier, C. J., Brandt, W. N., et al. 2019, ApJ, 872, 21
Hewett, P. C., & Foltz, C. B. 2003, AJ, 125, 1784
Hewett, P. C., & Wild, V. 2010, MNRAS, 405, 2302
Hopkins, P. F., & Elvis, M. 2010, MNRAS, 401, 7
Jiang, P., Zhou, H., Ji, T., et al. 2013, AJ, 145, 157
King, A., & Pounds, K. 2015, ARA&A, 53, 115
King, A. R., Zubovas, K., & Power, C. 2011, MNRAS, 415, L6
Kishimoto, M., Hönig, S. F., Beckert, T., & Weigelt, G. 2007, A&A, 476, 713
Knigge, C., Scaringi, S., Goad, M. R., & Cottis, C. E. 2008, MNRAS, 386, 1426
Krawczyk, C. M., Richards, G. T., Gallagher, S. C., et al. 2015, AJ, 149, 203
Krogager, J. K., Geier, S., Fynbo, J. P. U., et al. 2015, ApJS, 217, 5
Laor, A., & Draine, B. T. 1993, ApJ, 402, 441
Lee, J. C., Kriss, G. A., Chakravorty, S., et al. 2013, MNRAS, 430, 2650
Leighly, K. M. 2004, ApJ, 611, 125
Leighly, K. M., Dietrich, M., & Barber, S. 2011, ApJ, 728, 94
Leighly, K. M., Halpern, J. P., Jenkins, E. B., & Casebeer, D. 2007, ApJS, 173, 1
Leighly, K. M., Hamann, F., Casebeer, D. A., & Grupe, D. 2009, ApJ, 701, 176
Leighly, K. M., & Moore, J. R. 2006, ApJ, 644, 748
Leighly, K. M., Terndrup, D. M., Baron, E., et al. 2014, ApJ, 788, 123
Leighly, K. M., Terndrup, D. M., Gallagher, S. C., Richards, G. T., & Dietrich, M. 2018, ApJ, 866, 7
Leighly, K. M., Terndrup, D. M., Lucy, A. B., et al. 2019, ApJ, 879, 27
Lira, P., Kaspi, S., Netzer, H., et al. 2018, ApJ, 865, 56
Lucy, A. B., Leighly, K. M., Terndrup, D. M., Dietrich, M., & Gallagher, S. C. 2014, ApJ, 783, 58
Lynds, C. R. 1967, ApJ, 147, 396
Meusinger, H., Schalldach, P., Mirhosseini, A., & Pertermann, F. 2016, A&A, 587, A83
Meusinger, H., Schalldach, P., Scholz, R. D., et al. 2012, A&A, 541, A77
Miller, T. R., Arav, N., Xu, X., et al. 2018, ApJ, 865, 90
Netzer, H. 2013, The Physics and Evolution of Active Galactic Nuclei (Cambridge: Cambridge Univ. Press)
Netzer, H., Lutz, D., Schweitzer, M., et al. 2007, ApJ, 666, 806
Ogle, P. M., Cohen, M. H., Miller, J. S., et al. 1999, ApJS, 125, 1
Pilbratt, G. L., Riedinger, J. R., Passvogel, T., et al. 2010, A&A, 518, L1
Poglitsch, A., Waelkens, C., Geis, N., et al. 2010, A&A, 518, L2
Prevot, M. L., Lequeux, J., Maurice, E., Prevot, L., & Rocca-Volmerange, B. 1984, A&A, 132, 389
Proga, D., & Kallman, T. R. 2004, ApJ, 616, 688
Reichard, T. A., Richards, G. T., Hall, P. B., et al. 2003, AJ, 126, 2594
Richards, G. T., Lacy, M., Storrie-Lombardi, L. J., et al. 2006a, ApJS, 166, 470
Richards, G. T., Strauss, M. A., Fan, X., et al. 2006b, AJ, 131, 2766
Risaliti, G., Elvis, M., & Nicastro, F. 2002, ApJ, 571, 234
Rodríguez Hidalgo, P., Hamann, F., & Hall, P. 2011, MNRAS, 411, 247
Rogerson, J. A., Hall, P. B., Rodríguez Hidalgo, P., et al. 2016, MNRAS, 457, 405

Sabra, B. M., & Hamann, F. 2005, arXiv:astro-ph/0509421

Sanders, D. B., Soifer, B. T., Elias, J. H., Neugebauer, G., & Matthews, K. 1988, ApJL, 328, L35

Scannapieco, E., & Oh, S. P. 2004, ApJ, 608, 62

Schneider, D. P., Hall, P. B., Richards, G. T., et al. 2005, AJ, 130, 367

Smith, P. S., Schmidt, G. D., Allen, R. G., & Angel, J. R. P. 1995, ApJ, 444, 146

Sprayberry, D., & Foltz, C. B. 1992, ApJ, 390, 39

Sulentic, J. W., Marziani, P., & Dultzin-Hacyan, D. 2000, ARA&A, 38, 521

Thompson, T. A., Fabian, A. C., Quataert, E., & Murray, N. 2015, MNRAS, 449, 147

Tolea, A., Krolik, J. H., & Tsvetanov, Z. 2002, ApJL, 578, L31

Trump, J. R., Hall, P. B., Reichard, T. A., et al. 2006, ApJS, 165, 1

Urrutia, T., Becker, R. H., White, R. L., et al. 2009, ApJ, 698, 1095

Vacca, W. D., Cushing, M. C., & Rayner, J. T. 2003, PASP, 115, 389

Veilleux, S., Trippe, M., Hamann, F., et al. 2013, ApJ, 764, 15

Véron-Cetty, M.-P., Joly, M., & Véron, P. 2004, A&A, 417, 515

Violino, G., Coppin, K. E. K., Stevens, J. A., et al. 2016, MNRAS, 457, 1371

Voit, G. M., Weymann, R. J., & Korista, K. T. 1993, ApJ, 413, 95

Weymann, R. J., Morris, S. L., Foltz, C. B., & Hewett, P. C. 1991, ApJ, 373, 23

Wilson, J. C., Henderson, C. P., Herter, T. L., et al. 2004, Proc. SPIE, 5492, 1295

Zafar, T., Møller, P., Watson, D., et al. 2015, A&A, 584, A100

Zakamska, N. L., Sun, A.-L., Strauss, M. A., et al. 2019, MNRAS, 489, 497

Zhang, S., Ge, J., Jiang, P., et al. 2015, ApJ, 802, 92

Zubovas, K., & King, A. 2012, ApJL, 745, L34